

Contents lists available at ScienceDirect

Petroleum Science

journal homepage: www.keaipublishing.com/en/journals/petroleum-science



Original Paper

Establishing a fault sealing discrimination method to determine the optimal injection sites and injection rate for CO₂ storage in complex fault-block geological bodies



Zi-Yang Song $^{a, b}$, Lei-Lei Yang $^{a, b, *}$, Yi Liu $^{a, b}$, Fu-Jie Jiang $^{a, c}$, Xiao-Feng Li d , Zhen-Guo Qi $^{a, c}$, Zhen-Yuan Yin e

- ^a National Key Laboratory of Petroleum Resources and Engineering, China University of Petroleum (Beijing), Beijing, 102249, China
- ^b Unconventional Petroleum Research Institute, China University of Petroleum (Beijing), 102249, Beijing, China
- ^c College of Geosciences, China University of Petroleum (Beijing), Beijing, 102249, China
- ^d Exploration and Development Research Institute, Jiangsu Oilfield Company, SINOPEC, China
- ^e Institute for Ocean Engineering, Shenzhen International Graduate School, Tsinghua University, Shenzhen, 518055, Guangdong, China

ARTICLE INFO

Article history: Received 27 February 2024 Received in revised form 19 December 2024 Accepted 14 March 2025 Available online 20 March 2025

Edited by Jie Hao

Keywords:
CCUS
CO₂ geological storage
Fault-block geological bodies
Injection sites
Injection rate
CO₂ dissolution

ABSTRACT

The long-term stability of CO_2 storage represents a pivotal challenge in geological CO_2 storage (CGS), particularly within deep saline aquifers characterized by complex fault-block systems. While the injection sites and rate under different fault structures will directly affect the CO_2 storage effect and the risk of leakage. This study investigates the Gaoyou Sag in the Subei Basin, a representative fault-block reservoir, through an integrated numerical-experimental approach. A three-dimensional simulation model incorporating multiphase flow dynamics was developed to characterize subsurface CO_2 transport and dissolution processes. A novel fault seal capacity evaluation framework was proposed, integrating three critical geological indices (fault throw/reservoir thickness/caprock thicknesses) with the coupling of formation physical properties, temperature, and pressure for the rational selection of injection sites and rates. The results show that Optimal storage performance is observed when the fault throw is lower than the reservoir and caprock thicknesses. Furthermore, higher temperature and pressure promote the dissolution and diffusion of CO_2 , while compared to the structural form of faults, the physical properties of faults have a more significant effect on CO_2 leakage. The larger reservoir space and the presence of an interlayer reduce the risk of CO_2 leakage, and augmenting storage potential. Decreasing the injection rate increases the proportion of dissolved CO_2 , thereby enhancing the safety of CO_2 storage.

© 2025 The Authors. Publishing services by Elsevier B.V. on behalf of KeAi Communications Co. Ltd. This is an open access article under the CC BY-NC-ND license (http://creativecommons.org/licenses/by-nc-nd/4.0/).

1. Introduction

CO₂ geological storage (CGS) refers to the injection of CO₂ into depleted oil and gas reservoirs (Pacala and Socolow, 2004), deep saline aquifers, unminable coal seams, and the deep ocean (Rae et al., 2018; Liu et al., 2021, 2022; Han et al., 2022; Chen et al., 2022), to prevent CO₂ leakage and achieve permanent storage through four mechanisms, namely, structural capture, residual gas capture, dissolution capture, and mineral capture (Zhang and Song, 2014; Yang et al., 2010; Tang et al., 2020). As the global greenhouse effect intensifies, CGS technology has been recognized as a key tool

* Corresponding author. E-mail address: yangleilei@cup.edu.cn (L.-L. Yang). to combat greenhouse gas emissions and global warming (Li et al., 2024a, 2024b; Wang et al., 2024a, 2024b; Yang et al., 2023).

Generally speaking, aquifers in deep strata with high salinity (buried depth of more than 800 m) are not suitable for drinking water (Haszeldine, 2006). However, they possess a significant storage capacity and serve as the primary sites for CO₂ geological storage projects. Deep saline aquifers are typically located at greater depths in the ground, offering greater storage stability than the surface. Within these formations, faults are developed, and pore and fissure structures offer ample storage space (Qin et al., 2023). The complex fault-block structure of the geological body can provide favorable tectonic confinement conditions, although there is a risk of gas breakthrough and leakage through faults (Chen et al., 2024).

The safety and efficiency of long-term CO₂ storage in complex fault-block geologic bodies are influenced by various factors. These include the different stratigraphic and fault structures (Wang et al., 2023a), the physical properties of the stratigraphy and faults (Emad et al., 2018a; Gershenzon et al., 2015), the rate of CO₂ injection (Foroutan et al., 2022; Wang et al., 2023), the sites of CO₂ injection (Punnam et al., 2022; Wen et al., 2021), formation dip angle (Jing et al., 2023; Zhao et al., 2018), and non-homogeneity of reservoirs (Punnam et al., 2022). These conditions directly impact the long-term stability of CO₂ storage in the formation. CO₂ leakage would result in the failure of the CO₂ geological storage (CGS) project and pose safety risks.

The presence of faults possesses a dual nature in relation to CO_2 storage. On one hand, faults can create favorable tectonic trap conditions for CO_2 . On the other hand, faults may serve as potential leakage pathways that jeopardize the safety of CO_2 storage. Therefore, it becomes essential to investigate the impact of fault tectonics on CO_2 leakage. Recent studies by Jing jing (Jing et al., 2023) have highlighted the significance of temperature in controlling CO_2 leakage along faults within fault-developed strata. Additionally, Miocic (Johannes et al., 2019) has discussed the potential risk of CO_2 leakage back to the surface through geological faults, which can pose a substantial threat to the integrity of CO_2 storage.

Previous studies have mostly focused on the impact of a single control factor or a single fault on CO₂ storage. Many of these studies have utilized idealized numerical simulations that overlook the heterogeneity present in actual formation structures. For instance, Hodneland and Al-Khdheeawi (Emad et al., 2018b; Erlend et al., 2019) investigated the impact of temperature on CO₂ storage efficiency and migration but did not account for the influence of formation heterogeneity and fault structures. Bu and Yang (Bu et al., 2016; Yang et al., 2018) examined the safety and leakage risks associated with faults in CO₂ migration while neglecting the influence of temperature on CO₂ geological storage. However, there is no research that can determine the optimal injection sites and rate based on the structural characteristics and physical properties of actual fault-block traps for CO₂ storage (Li et al., 2024a, 2024b; Wang et al., 2024a, 2024b; Song et al., 2024).

In this study, the Gaoyou Sag in northern Jiangsu Province was selected as the research area. A set of large-scale non-homogeneous models was established to reconstruct the actual geological profile, along with three sets of small-scale models representing the typical fault structures within the sag. The CO₂ storage capacity of different fault structures has been simulated and analyzed using TOUGH2-ECO2N, and a set of evaluation methods for CO₂ storage capacity of fault block geologic bodies has been established. On this basis, the safe injection sites and injection rate of CO₂ were elucidated on a practical field scale using a large-scale model and the main control factors of CO₂ diffusion, dissolution and leakage were explored.

2. Geological background

The Subei Basin is situated in northern Jiangsu, China, and in the northern region of the Yangtze Plate. Within the basin, there exists a north-to-south geological arrangement consisting of the Yanfu depression, Jianhu uplift, and Dongtai depression. The Gaoyou sag, located in the central-southern part of the Dongtai depression, is notably characterized by its abundant reserves of oil and gas resources (Qiao et al., 2012).

The Upper Cretaceous Taizhou Formation-Neogene strata covered by the Quaternary in Gaoyou Sag are widely developed. They are Chishan Formation (K_2c) , Taizhou Formation (K_2t) , Funing Formation (E_1f) , Dainan Formation (E_2d) , Sanduo Formation (E_2s) and Yancheng Formation (Ny) from bottom to top $(Zhou\ et\ al.,$

2019). According to logging and lithology, Taizhou Formation can be divided into two sections vertically, which are called the first member of Taizhou Formation (K_2t_1) and the second member of Taizhou Formation (K_2t_2) from bottom to top (Fig. 1). The lithology of K_2t_1 is pebbly sandstone, fine sandstone, silty mudstone and mudstone. The lithology of the lower part of K_2t_2 is gray black and dark gray mudstone with thin layer of light gray siltstone. The K_2t_1 and K_2t_2 formations form a set of reservoir-caprock assemblages that are conducive to CO_2 geological storage (Liu et al., 2016; Gao et al., 2018).

3. Numerical simulation

3.1. Modeling tool

Different from the traditional numerical simulation software Feflow and abaqus, TOUGH2 simulator combined with ECO2N module is used in this study. The TOUGH2 simulator is one of the best known and most widely used multi-component multiphase flow simulation software in the world today. TOUGH2 is based on mathematical and physical equations to model multiphase flow (water, gas, steam) and multiphase heat transfer (conduction, convection, radiation) in subsurface media. It can be used to model engineering and scientific problems such as geothermal energy utilization, carbon dioxide storage, and groundwater pollution transport (Yang et al., 2013). The TOUGH2-ECO2N program is developed on the basis of TOUGH2, which is a numerical simulator specifically applied to CO₂ geological storage, in which the module of ECO2N (Gherardi et al., 2007) is specialized to deal with threephase systems (gas, liquid and supercritical phases) as well as three-component (water, salt and CO₂) systems in which CO₂ is in different pressure and temperature conditions.

In recent years, several researchers verified the accuracy of the TOUGH2-ECO2N by comparing the solubility of CO₂ in water under different temperature and pressure changes, different phase states, and different salinities through experiments and simulations (Pruess and Spycher, 2007; Shabani and Vilcáez, 2018). At the same time, validation was also conducted on the issue of CO₂ diffusion model (Spycher and Pruess, 2005) to ensure the reliability of simulation results, and has been widely used (Xu et al., 2006).

Mathematical equations for flow and transport. All flow and transport equations have the same structure, and can be derived from the principle of mass (or energy) conservation. Governing equations involved are tabulated in Table 1.

3.2. Geological model

The geological model presented in Fig. 2 is established based on seismic logging data, utilizing a representative section from the Chenbao area in Gaoyou sag. The selected section lies between Chen 2 well and Chen 3 well. The model features a significant number of synthetic faults, including the Wu 1 fault and Wu 2 fault. The model has dimensions of 6400 m in length, with a top depth of 1155 m and a bottom depth of 3478 m. It comprises ten formations and three sets of reservoir-caprock assemblages from top to bottom. Among these, the K_2t_1 , E_1f_1 , and E_1f_3 formations have been identified as suitable CO₂ reservoirs due to their favorable porosity, permeability, and extensive storage capacity. Moreover, the upper part of these reservoirs is characterized by a low-porosity and lowpermeability caprock and fault, which effectively inhibit CO2 leakage and migration. While the K_2t_2 , E_1f_2 , and E_1f_4 formations serve as effective mud shale caprocks, with thicknesses ranging from 100-150 m, 100-300 m, and 40-120 m, which are good for the sealing of the CO_2 .

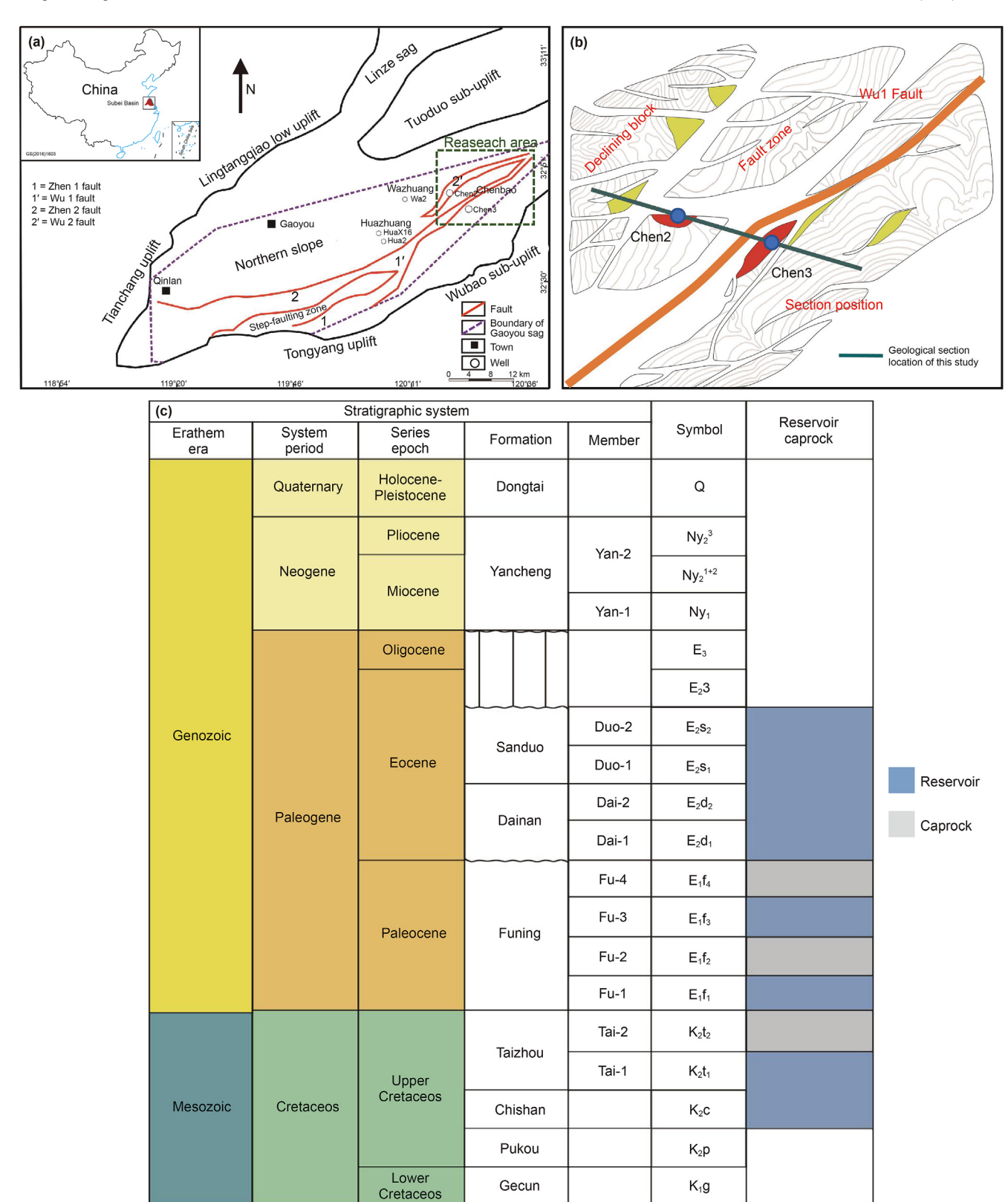


Fig. 1. Location map of the GaoYou sag in North Jiangsu Basin. (a) Location of the research area; (b) The location of the geological section used by the model; (c) Detailed stratigraphy, reservoir-seal assemblage of the Ny₂–K₁g.

 Table 1

 Governing equations involved in the reactive transport simulation.

Governing equations	Symbols
Fluid and heat flow: General governing equations: $\frac{\partial M_k}{\partial t} = -\nabla F_k + q_k$ $u_\beta = -K \frac{K_{r\beta}}{\mu_\beta} (\nabla P_\beta - \rho_\beta g)$ Water: $M_w = \phi(S_l \rho_l X_{wl} + S_g \rho_g X_{wg})$ $F_w = X_{wl} \rho_l u_l + X_{wg} \rho_g u_g$ $q_w = q_{wl} + q_{wg}$ $CO_2:$ $M_c = \phi(S_l \rho_l X_{cl} + S_g \rho_g X_{cg})$ $F_c = X_{cl} \rho_l u_l + X_{cg} \rho_g u_g$ $q_c = q_{cl} + q_{cg}$	M: mass accumulation, kg·m ⁻³ t: time, s F: mass flux, kg·m ⁻² ·s ⁻¹ q: source/sink u: Darcy velocity, m·s ⁻¹ K: permeability, m ² K _r : relative permeability P: pressure, Pa g: gravitational acceleration, m·s ⁻² S: saturation ρ: density, kg·m ⁻³ X: mass fraction φ: porosity μ: viscosity, kg·m ⁻¹ ·s ⁻¹ Subscripts: k: governing equation index β: phase index w: water c: CO ₂ g: gas phase
	l: liquid phase

Since the displacement pressure of the reservoir after CO2 injection approximates or even exceeds the displacement pressure of the fault, previous studies have shown that the fault cannot be closed at this time and behaves as a high-porosity permeability fault. The capacity of faults to sequester CO₂ relies significantly on three key parameters: reservoir thickness, caprock thickness, and fault throw. To investigate the influence of these three factors on CO₂ storage within complex fault-block geological bodies, the geological structure of representative fault-block formations in the geological model is refined. Three small-scale models with typical fault characteristics were established: the two sides of the sealing fault are sandstone and mudstone respectively, the two sides of the sealing fault are both sandstone, the two sides of the sealing fault with small fault dip angles are sandstone and mudstone respectively (Fig. 2). The favorable conditions for CO₂ storage were determined, serving as a fundamental basis for the identification and selection of CO₂ injection sites within large-scale models.

3.3. Conceptual model

3.3.1. Small-scale models

During the implementation of CGS engineering within intricate fault-block geological formations, the primary mechanism for $\rm CO_2$ retention is to confine it within structural traps. Therefore, it is very important to clarify the influence of fault-block types and structural characteristics of main storage sites on $\rm CO_2$ migration. Based on previous studies, the efficacy of the coupled reservoir control model, incorporating fault throw, reservoir thickness, and caprock thickness, has been extensively demonstrated in fault-block oil and gas reservoirs, showcasing its robustness and reliability. Moreover, this control model exhibits applicability in evaluating the $\rm CO_2$ storage capacity potential within intricate fault-block geological formations.

In section 3.2, based on the actual seismic and logging data, a geological model was established in the Chenbao area of Gaoyou Sag, and three small-scale models with different fault-block traps were selected according to the coupling situation of fault, reservoir, caprock. Based on the geological model, according to its typical structural form, the model is generalized and the corresponding numerical model is established. The numerical models are used to determine the influence of fault throw, reservoir thickness and caprock thickness on $\rm CO_2$ storage capacity in complex fault-block geological bodies. It provides a basis for the selection of reasonable injection sites of $\rm CO_2$.

The size of the model is 100 m \times 75 m \times 10 m, 100 grids are divided in the X direction, 75 grids are divided in the Z direction, and 1 grid is divided in the Y direction. The size of each grid is 1 m \times 1 m \times 10 m, and the geological structure contained in the interior is the same as that of the geological model. The specific values of fault throw (L), reservoir thickness (R) and caprock thickness (M) of the model are shown in Fig. 3.

3.3.2. Large-scale models

Numerical simulation model was constructed in accordance with the geological model formulated in Section 3.2. The large-scale model encompasses an identical number of strata and faults as the geological model, with dimensions of 6400 m in the X-direction and a depth of 2323 m in the Z-direction (Fig. 4).

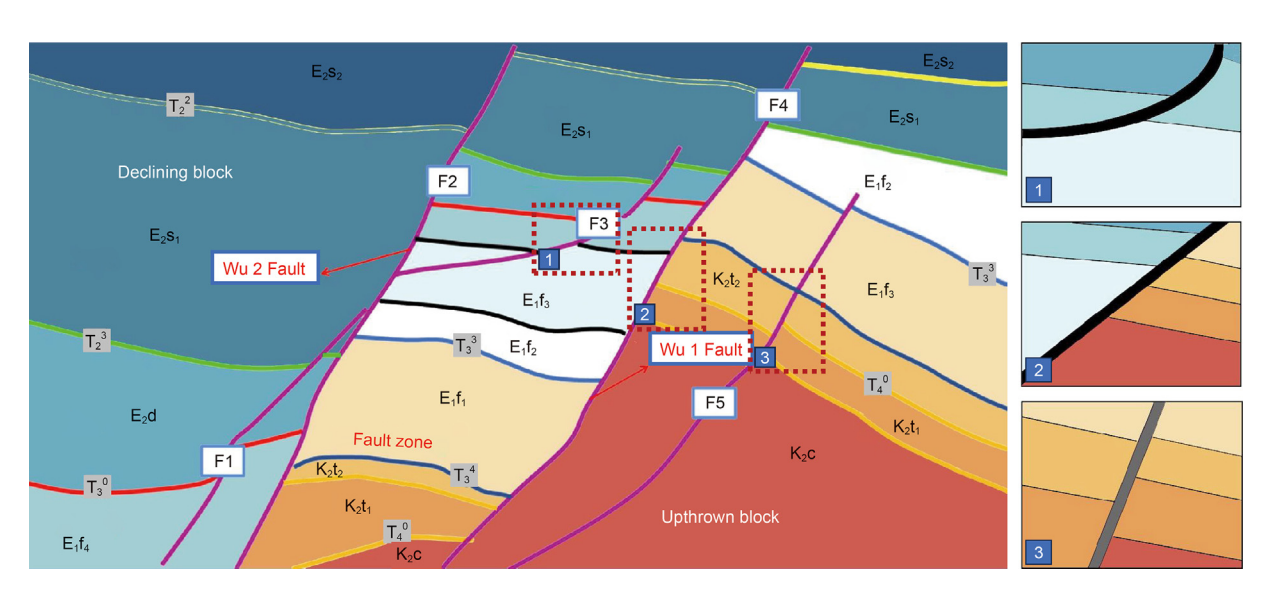


Fig. 2. Schematic diagram of geological model and small-scale model in Chenbao Area, Gaoyou Sag, Subei Basin.

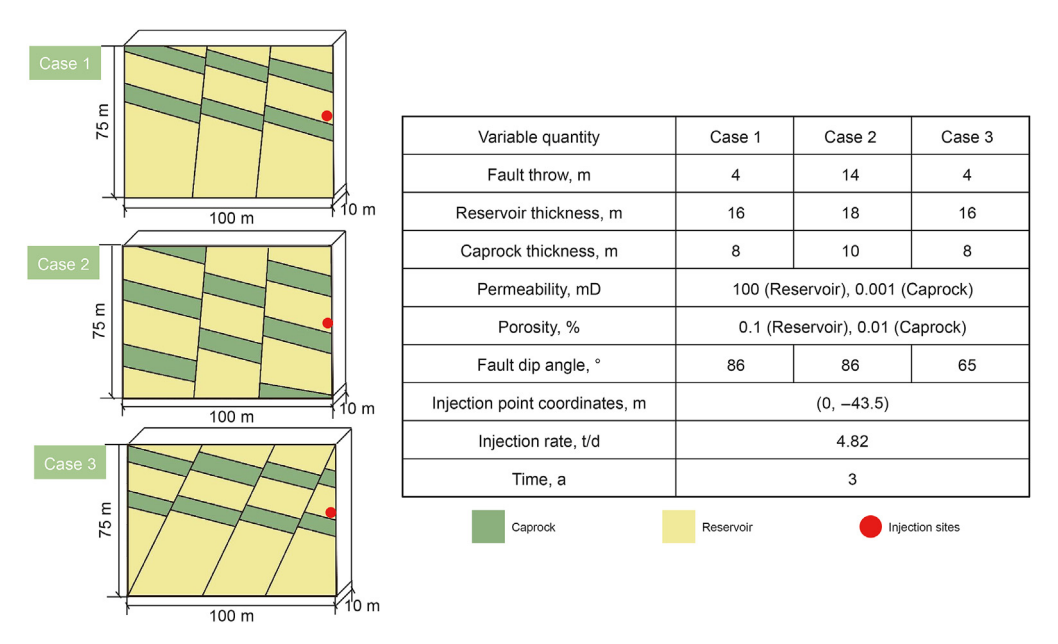


Fig. 3. Small-scale model of typical fault structure and model basic parameters.

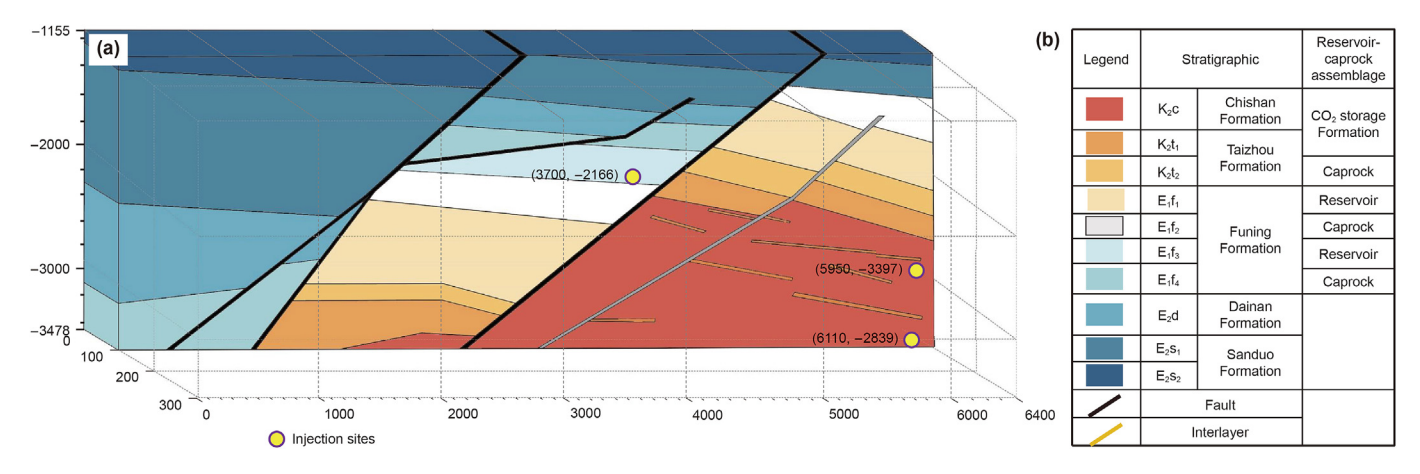


Fig. 4. Conceptual model:(a) 3D schematic; (b) Introduction of model strata and reservoir-caprock combination.

Subsequently, a meticulous mesh division was implemented. The horizontal section was discretized into 320 cells with a uniform grid length of 20 m, while the vertical section was divided into 100 cells with a consistent grid height of 23.23 m. The fault grid is subdivided by three rows of grids, with the fault grid in the center and the boundary grid on both sides.

3.4. Initial condition

3.4.1. Stratigraphic conditions

The model involves 10 stratigraphic groups and 5 faults of Chishan Formation (K_2c), Taizhou Formation (K_2t_1 , K_2t_2), Funing Formation (E_1f_1 , E_1f_2 , E_1f_3 , E_1f_4), Dai'nan Formation (E_2d), Sanduo Formation (E_1s_1 , E_1s_2). Porosity and permeability ranged from 22.1–0.36% and 345.6–0.001 mD, respectively (Fig. 5). Three groups of caprock, K_2t_1 , E_1f_2 , and E_1f_4 , have low porosity and permeability. Porosity is 0.36% and permeability is 0.001 mD. The two sets of caprock thickness intervals mainly involved in this simulation are E_1f_4 : 151–225 m K_2t_2 :194–237 m. In contrast, the

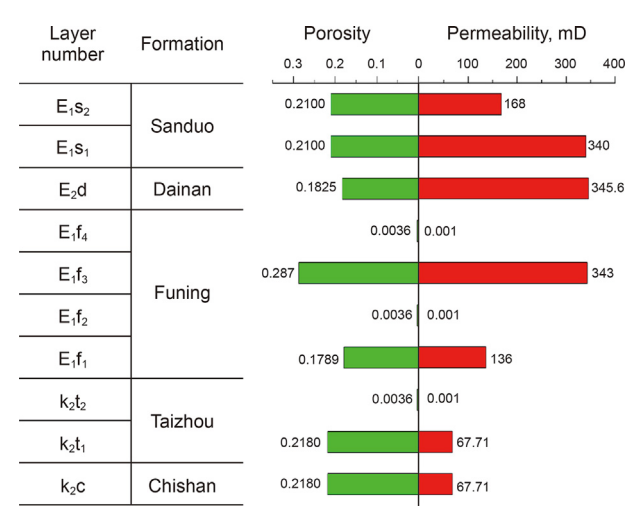


Fig. 5. The porosity and permeability of the formation in the model.

 K_2c , K_2t_1 , and E_1f_1 reservoirs have better physical properties and are used for CO_2 geological storage.

3.4.2. Initial temperature and pressure conditions

The initial formation pressure was determined based on pressure monitoring of the actual formation. Based on the actual formation pressure gradient of 0.94 MPa/100 m, the initial pressure field of the model was established with a top pressure of 7.05 MPa and a bottom pressure of 29.09 MPa. The temperature gradient in the region was obtained from the actual monitoring data as 2.79 °C/100 m and combined with the interpolation algorithm to obtain the initial temperature data for the entire modeled region. The temperature at the top of the model is 45 °C and the temperature at the bottom is 110 °C.

3.4.3. Fault

With the increase of fault throw, ductile clay may be brought into the fault and applied to the contact surface, resulting in mudstone smearing, which subsequently decreases fault porosity and permeability (Zheng and Espinoza, 2022). Mudstone smearing is a prevalent geological phenomenon observed in the fault zones. During fault activity, the high plasticity of mudstone allows it to invade fault plane and block their pores under the influence of compressive stress or gravity. Additionally, mudstone may undergo varying degrees of dynamic metamorphism, leading to the densification of components within the mudstone coating layer and resulting in fault sealing (Ciftci et al., 2013; Noorsalehi-Garakani et al., 2013).

In small-scale models, since the displacement pressure of the reservoir after CO_2 injection approximates or exceeds the displacement pressure of the fault, the fault cannot be sealed and behaves as a high-porosity permeability fault. The physical properties of the fault are not the dominant factor for sealing, and the sealing of the fault depends on the fault structure. Therefore, the porosity and permeability of the fault in the reservoir are set to 10% and 100 mD.

In large-scale models, 5 faults are developed, and their positions and shapes are shown in Fig. 4. The faults F2, F3, and F4, which exhibit longer sliding distances, demonstrate a more pronounced mudstone smear phenomenon, resulting in lower internal porosity and permeability. These faults can be classified as sealing faults, with porosity and permeability values of 0.36% and 0.001 mD, respectively. In addition, faults F1 and F5, characterized by shorter sliding distances, display less noticeable mudstone smearing phenomena. Consequently, these faults exhibit good physical properties, with porosity and permeability values of 15% and 60 mD, respectively. The fault grids are individually linked together to ensure the basic characteristics of a sparse and blocking fault, and the two side grids are linked to the middle fault grid respectively, allowing for fluid transport between them. The K₂c Formation is found to contain a significant abundance of mud shale interlayers, which exhibit low porosity and permeability values of 0.09% and 0.001 mD, respectively.

3.4.4. Boundary condition

Based on previous research on CO_2 geological storage and the influence of model boundaries on numerical solutions. In large-scale geological model, the lateral boundaries were implemented as the primary boundary condition with constant pressure and temperature. Meanwhile, the upper and lower surface boundaries were designated as zero-flow conditions.

In the small-scale model of the influencing factors of CO_2 geological storage, When the local pressure is too large due to excessive injection of CO_2 , the model will not be able to operate normally. Moreover, finite boundary models fail to accurately represent changes in the true CO_2 flow behavior. To address these

limitations, this study extends the left boundary of the model to an infinite volume. Under the assumption of infinite volume, the left boundary no longer has a direct influence from external inflows or outflows, which means that CO₂ transport is mainly controlled by internal dynamics (e.g., diffusion due to concentration gradients) and fluid flow (e.g., convection). This ensures a realistic flow environment within the formation that aligns with the CO₂ flow dynamics.

3.4.5. Injection condition

In this simulation, the injection methods are all single mesh injections, so the mesh size determines the length of the injection site, which is 1m in the small-scale model and 20 m in the large-scale model. In the small-scale model, the injection site coordinates are (0, -43.5), the injection rate is 4.32 t/d, the injection time is 0.2 year, and the simulation time is 3 years. In a large-scale model, three injection sites (3700, -2166), (6110, -2839), and (5950, -3397) were set up for simulation, as well as three different injection rates of 523, 400, and 350 t/d. The injection time of the model is 10 years, and the simulation time is 500 years. The CO_2 injection method for both small-scale and large-scale models is constant flow rate injection (Table 2).

3.5. Model solutions

This research initially constructed three small-scale models to investigate the CO_2 sealing capacity of three typical fault configurations in complex fault-block geological bodies of Gaoyou Sag, and proposed two fault structure shapes that can partially store CO_2 . Subsequently, choosing F3, F4, and F5 faults with these two types of fault structures to form CO_2 storage traps with the overlying layers. In the reservoirs E_1f_4 , K_2c , and K_2t_1 below the three faults, combined with the influence of depth and interlayer. Three rational injection sites (3700, -2166), (6110, -2839), and (5950, -3397) were selected to evaluate the influence of distinct injection sites on CO_2 migration and storage, and determine the optimal injection sites. Finally, in order to prevent CO_2 leakage along faults, various injection rates of 523, 400, and 350 t/d were considered to ascertain the most suitable injection rate for secure CO_2 storage (Table 2).

4. Result

4.1. Distribution of CO₂ under small-scale models

 CO_2 is injected from the lower right side of the reservoir and transported upward by buoyancy. The presence of the caprock on both sides of the fault effectively blocks the CO_2 transport. As illustrated in Fig. 6(a)—(c), If the two sides of the fault are sandstone and mudstone respectively (R, M > L), the CO_2 will initially accumulate beneath the fault and caprock. The mudstone caprock on the left side of the fault, with its low porosity and permeability, effectively seals the CO_2 migration. However, as CO_2 is injected, the formation pressure will continue to increase. When the local formation pressure exceeds the breakthrough pressure of the fault, the CO_2 will continue migrating to the left across the fault. Eventually, a portion of the CO_2 can be retained beneath the fault.

When the dip angle of the fault decreases, in Fig. 6(g)—(i), it can be observed that the fault can accommodate a larger amount of CO_2 , resulting in increased space for CO_2 enrichment in the right reservoir. The filling of CO_2 under the fault and caprock takes longer, after which it continues to migrate towards the left. The smaller fault dip angle provides enhanced stability for CO_2 enrichment, ultimately leading to a higher retention of CO_2 under the fault.

When the two sides of the fault are both sandstone (R > L > M), the sandstone reservoir on the left side cannot effectively seal the

Table 2Summary of the simulation scenarios.

Case	Model dimension (X \times Y \times Z)	Injection sites coordinates, m	Injection rate, t/d	Injection time, a	Model other parameters
1 2 3	100 m × 10 m × 75 m	(0, -43.5)	4.32	0.2	Porosity, permeability, and the relationship between fault throw, reservoir thickness, and caprock thickness are shown in Fig. 3.
4 5 6 7 8	6400 m × 100 m × 2323 m	(3700, -2166) (6110, -2839) (5950, -3397) (5950, -3397) (5950, -3397)	523 400 350	10	Porosity, permeability are actual measured values, as shown in Fig. 5.

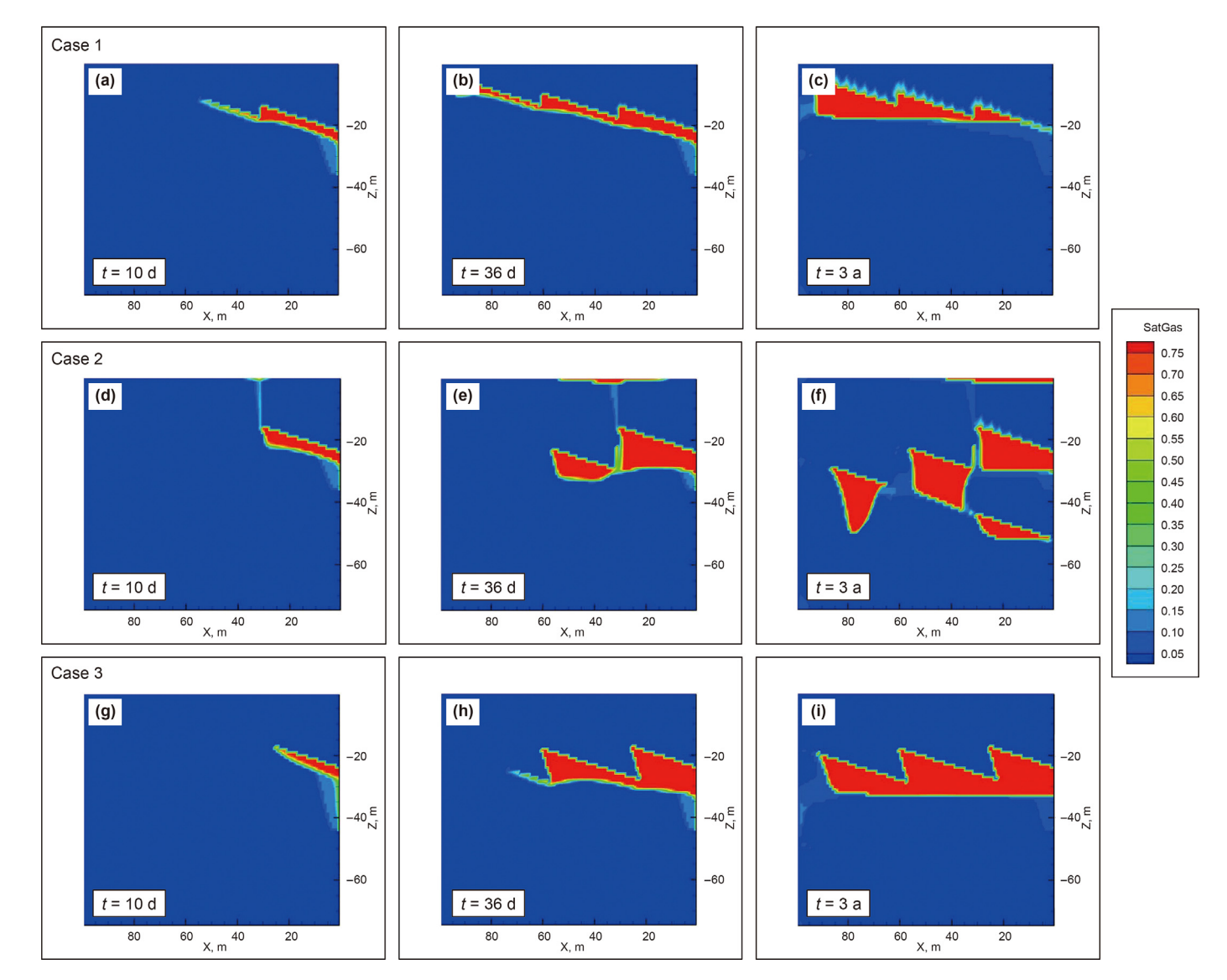


Fig. 6. Distribution of CO₂ after injection under small-scale models. "SatGas" denotes gas saturation.

 CO_2 , providing a pathway for upward transport and leakage of CO_2 , CO_2 has a tendency to move upwards through this channel. As depicted in Fig. 6(d)—(f), when CO_2 is still injected from the injection sites on the right side of the model (0, -43.5), CO_2 has a tendency to migrate to the left. When the injection rate is greater than the rate at which CO_2 leaks upwards from the channel, partial CO_2 will still accumulate below the cap layer on the injection side. As CO_2 accumulates below the right caprock, when the depth of accumulated CO_2 exceeds the thickness of the left caprock, CO_2 will

continue to migrate and diffuse to the left. This fault structure is unstable for CO₂ storage and is prone to trigger leakage.

4.2. Injecting CO_2 at different positions and rates in large-scale models

4.2.1. Injection sites selection

In Section 4.1, three representative structures within complex fault-block geological formations were selected for rigorous

simulation analysis. The obtained results highlight the pivotal role played by geological structures in influencing the storage capacity and safety considerations pertaining to CO₂ storage. To further investigate the Coupling effect of different injection sites and geological structures on CO₂ geological storage within the selected study area, as well as to identify optimal injection sites for CO₂ geological storage. This study selected three significant injection sites based on the simulation outcomes in Part 4.

The specific locations and geological structures of the three injection sites determined are as follows: In Case 4, the injection site (3700, -2166) is situated beneath the F3 sandstone-mudstone connection fault within the reservoir E_1f_3 . Notably, this fault exhibits a substantial dip. In Case 5, the injection site (6110, -2839) is located in the upper section of the K_2c reservoir, positioned below the right side of the F5 sandstone-mudstone connection fault. This particular fault demonstrates a minor dip, along with the presence of interlayer above the injection sites. Finally, in Case 6, the injection site (5950, -3397) is situated in the lower part of the K_2c reservoir. Above the injection sites, the K_2c reservoir exhibits widespread development of interlayers, while the left is the F4 sandstone-sandstone connection fault.

4.2.2. Pressure evolution of CO₂ injection at different sites

Case 4 simulation (Fig. 7(a)–(f)) results show that when CO_2 is injected into the E_1f_3 formation for 1–10 years, an overpressure zone will be formed in the E_1f_3 reservoir. However, the stable sandstone–mudstone connection fault F3 effectively impedes pressure breakthrough, minimizing its propagation across the fault, Pressure cannot leak. Merely a small portion of the pressure seeps through the F3 fault. The formation pressure at the injection site before injection was 1.67×10^7 Pa, and the maximum pressure after injection reached 5.65×10^7 Pa, and the pressure ratio before and after injection reached 3.38, which is unsafe. As CO_2 injection ceases after 10 years, the pressure within the E_1f_3 gradually diminishes, aligning with the pressures on the left and right sides.

The simulation results of Cases 5 and 6 reveal a similar pressure evolution trend when CO₂ is injected into the K₂c formation, regardless of whether the injection occurs in the upper or lower part of the formation (Figs. 8(a)–(f), 9(a)–(f)). The presence of interlayer in the K2c formation has negligible impact on CO2 injection. In 0-3 years, due to the injection of CO_2 , the pressure of the formation within the right region increases. The F4 sealing fault partially inhibits the transmission of pressure, resulting in insignificant changes in pressure within the middle and left regions of the formation during this period. With the continuous injection of CO₂, the F4 fault was broken by pressure in 3-10 years, and the pressure in the middle part of the formation increased rapidly, and the upper caprock E₁f₂ and E₁f₄ blocked the upward transmission of pressure. An overpressure zone materializes in the lower right section of the model. The maximum formation pressure before injection was 2.908×10^7 Pa, and the maximum formation pressure after injection was 5.806×10^7 Pa, at which time the pressure ratio before and after injection was 2.0, and was reduced to 4.40×10^7 Pa at the location where CO₂ broke through the F4 fault. Compared to Case 4, this pressure ratio is lower and relatively safer. However, considering the leakage of CO₂ along faults and formation overpressure, it is necessary to adjust the injection rate to make CO₂ injection and storage safer. Subsequently, with the stop of CO₂ injection, the formation pressure gradually decreases, and the pressure on the left and right sides tends to be consistent.

4.2.3. Supercritical CO₂ distribution with different injection sites

In the CO_2 geological storage project, evaluating the safety of CO_2 storage relies heavily on understanding the migration pattern of supercritical CO_2 . In Case 4 (Fig. 7(g)—(1)), the presence of a

sandstone-mudstone connections on both sides of the F3 fault, combined with a significant fault dip angle, ensures a stable fault condition. Over a span of 500 years, the supercritical CO_2 becomes concentrated in the E_1f_3 area, spreading along the F3 fault and the E_1f_4 caprock, without any noticeable leakage.

In Case 5 (Fig. 8(g)—(1)), following the initiation of CO_2 injection within O-1 year, the CO_2 was obstructed by the interlayer above. However, a small amount of CO_2 eventually accumulated below it. The remaining CO_2 continued its upward movement. In the 10th year, the CO_2 reaches the caprock of K_2t_2 and accumulates beneath it. Although the sandstone-mudstone connection exists on both sides of the F5 fault. Due to the minimal mudstone smear distance caused by the sliding of the fault's two sides, the F5 fault exhibits high porosity and permeability. Consequently, when the CO_2 reaches the intersection of the F5 fault and the K_2t_2 caprock, it tends to continue its upward movement along the fault. Between 10 and 500 years, some CO_2 migrates upward along the F5 fault, reaching the lower part of the E_1f_2 caprock. The final CO_2 enrichment area is below the interlayer in the K_2c reservoir, the K_2t_1 reservoir, and the E_1f_1 reservoir.

Because the injection site of Case 6 is located at the bottom of the K_2c reservoir (Fig. 9(g)–(1)), in the early 1–30 years, CO_2 will migrate in the K_2c formation and do not reach the fault, so the overall migration trend is more secure. Due to the existence of interlayers in the K_2c formation, the trend of CO_2 lateral migration is more obvious, and the reservoir space can be more fully utilized, which makes some CO_2 stay below the interlayers and eventually stored. In 100 years, the CO_2 migrated to the intersection of the F4 fault and the K_2t_2 caprock, and then in 100-500 years, the F4 sandstone-sandstone connection fault with weak stability was broken through, and a small amount of CO_2 migrated upward. Finally, it was blocked by the E_1f_4 caprock and stored in the E_1f_3 fault. The final enrichment area of CO_2 is below the interlayer in K_2c reservoir, K_2t_1 reservoir and E_1f_3 reservoir.

4.2.4. CO₂ injection at different injection rates

In Sections 5.2 and 5.3, the simulation results in Case 6 show that although the left side of the injection site is a sandstone connection fault with poor fault stability, the K_2c reservoir space can be fully utilized at the bottom of the K_2c reservoir, and the total amount of CO_2 that can be held in its reservoir is larger than the total amount of CO_2 that can be injected at the injection sites of Case 4 and Case 5. At the same time, the CO_2 leaked by Case 6 along the F4 fault is also blocked by the E_1f_4 caprock in the middle of the formation and no leakage occurred. Therefore, the injection site of Case 6 can accommodate more CO_2 , and the storage safety of CO_2 is good. At the same time, the higher temperature and pressure at the injection site favour CO_2 storage in the dissolved phase, which makes the injection site at Case 6 a more desirable site for CO_2 injection in the region. The effects of temperature and pressure on CO_2 storage are discussed in Section 5.2.1.

After determining the reasonable injection sites, a study is conducted to explore the direct impact of CO_2 injection rate on CO_2 geological storage and to determine the appropriate CO_2 injection rate in this area. In this study, three groups of Case 6, Case 7 and Case 8 were compared, and the injection rates were 523, 400 and 350 t/d, respectively. To explore the control effect of CO_2 injection rate on CO_2 migration and final CO_2 geological storage effect.

In Fig. 9(g)–(1), at an injection rate of 523 t/d, a more significant CO_2 leakage occurs. The CO_2 breaks through the F4 sandstone-sandstone connection fault and gets transported upward, enriching below E_1f_4 . At a lower CO_2 injection rate of 400 t/d (Fig. S2(a)–(f)), less CO_2 accumulates under the F4 fault after 100 years. The trend of CO_2 breaking through the F4 fault slows down significantly compared to Case 6. When the CO_2 injection rate is further reduced

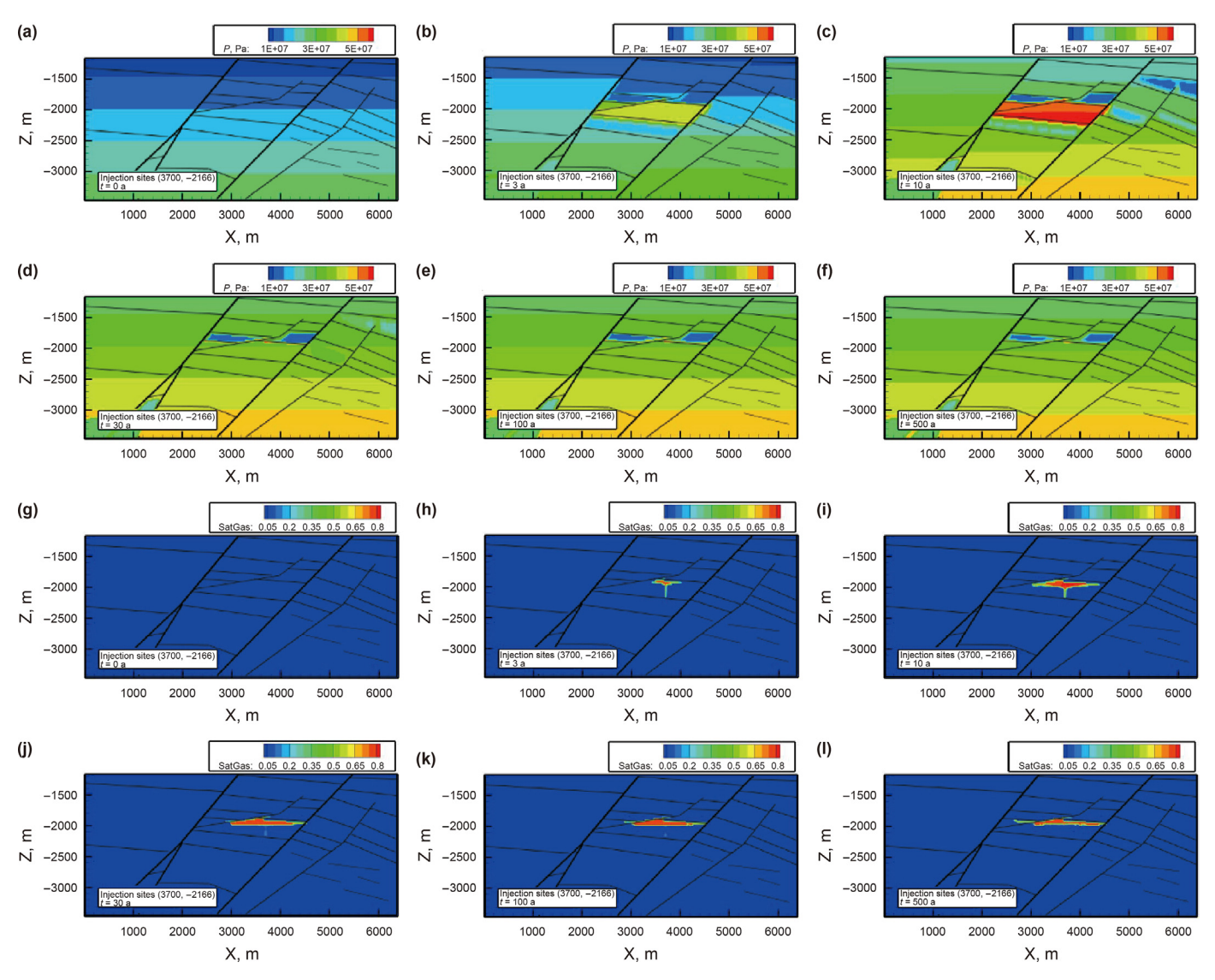


Fig. 7. The formation pressure and CO_2 migration at the injection site (3700, -2166).

to 350 t/d (Fig. S2(g)–(1)), the CO₂ is transported below the F4 fault, but there is no obvious breakthrough or upward transportation. And when the injection rate is 350 t/d, the pressure monitoring results show that the pressure at the injection sites before injection is 2.91×10^7 Pa, and the pressure at the injection sites after injection is 4.93×10^7 Pa, at which time the pressure ratio before and after injection is 1.69 (Fig. 10). This pressure is smaller and safer than the pressure generated by the injection rate of 523 t/d.

5. Discussion

5.1. Coupling of fault characterization and fault physical properties for geological storage of CO_2

The influence of fault characteristics on the geological storage of CO₂ encompasses a multitude of factors, such as fault inclination, fault distance, and fault strike. This article focuses on analyzing the impact of three factors, "fault throw—reservoir thickness—caprock thickness" and fault dip angle on the sealing of faults. Meanwhile, the injection of CO₂ at various sites in large-scale models also reflects the significant influence of faults physical properties on the storage and transportation of CO₂.

In Fig. 6(a)—(c), the two sides of the synthetic fault are sandstone and mudstone respectively when the fault throw (L) is smaller than both the reservoir thickness (R) and caprock thickness (M). In this scenario, whether the fault has high porosity and permeability or acts as a lithology seal with low porosity and permeability, the area below the fault and caprock can contribute to CO_2 storage. The total amount of CO_2 storage depends on the fault throw and the fault dip angle. As depicted in Fig. 6(g)—(i), a decrease in fault dip angle leads to an increase in the capacity of CO_2 retention below the fault.

When R > L > M (Fig. 6(d)—(f)), the two sides of the synthetic fault are sandstone and sandstone respectively, the fault does not have the ability to sequester CO_2 . Although the CO_2 can diffuse around, there is still a small amount of residual CO_2 enrichment below the caprock. This observation highlights the fact that the presence of interlayers that act as local caprocks can enhance the CO_2 storage capacity. When choosing CO_2 injection sites, it is also feasible to consider injecting them into reservoirs that have developed interlayers.

In addition to the two cases mentioned in the article, Case 1 and Case 2, we also explored several other potential combinations of L, M, and N. The results of the simulations and CO_2 storage capacity

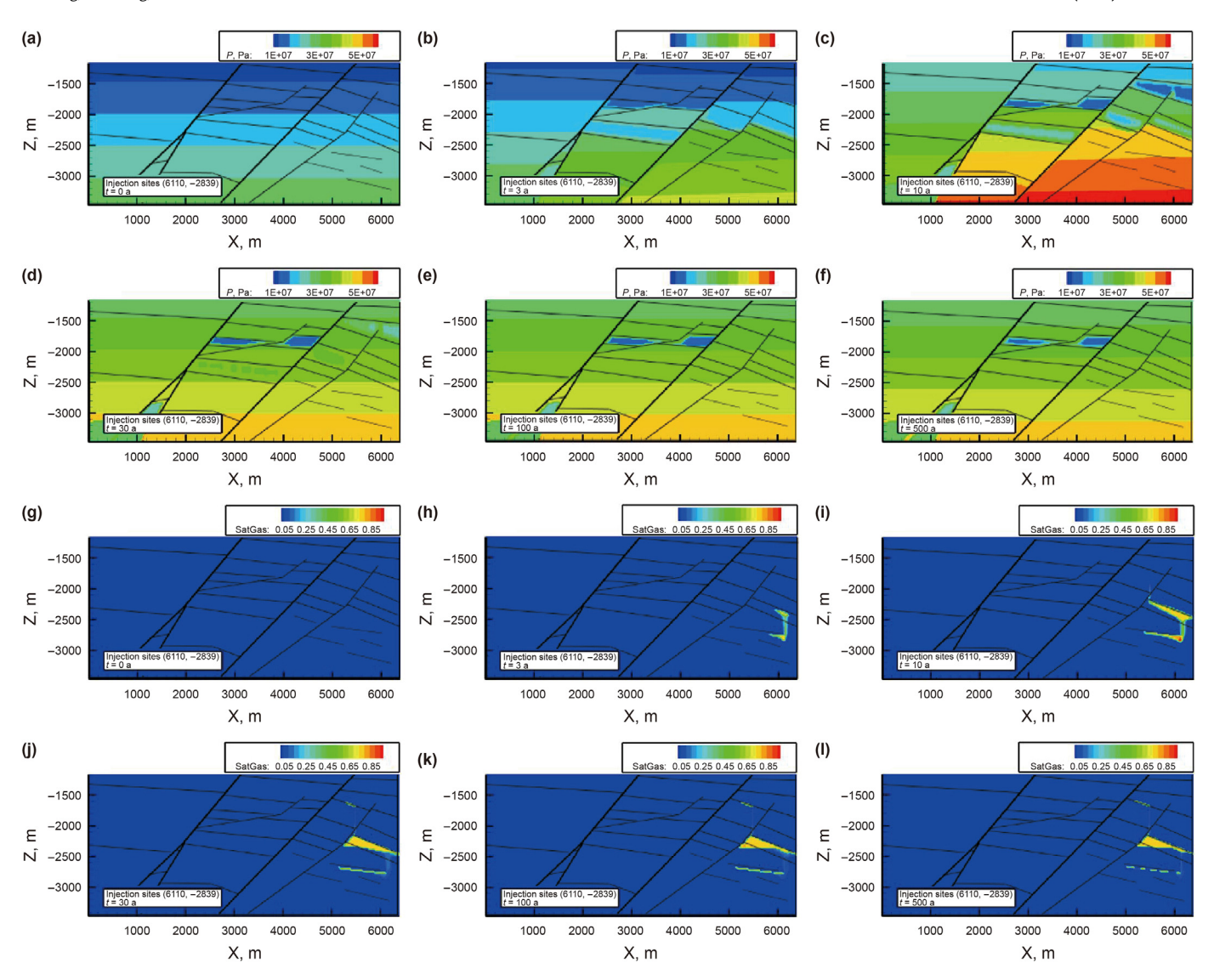


Fig. 8. The formation pressure and CO_2 migration at the injection site (6110, -2839).

can be found in Fig. S1. Based on the simulation results, a triangle diagram is drawn to divide the fault's CO₂ storage capacity into four types, depending on the relationship between L, M, and N (Fig. 11): Completely sealed, partial sealed, unable to seal, and unable to seal (small amount of CO₂ remaining).

However, the simulation results of the large-scale model (Fig. 9(1)) indicate that, in addition to the structure characteristics of the fault, the physical properties of the fault also play a significant role in CO₂ storage. Although both sides of the F4 fault are sandstone, the porosity and permeability of the F4 fault are relatively low, and the large-scale CO₂ escaping did not occur like Case 2 (Fig. 6(d)–(f)) after CO₂ reaching the F4 fault, and most of the CO₂ is still enriched underneath the F4 fault. While injecting under the F5 fault (Fig. 8(1)), although the two sides of the fault are sandstone and mudstone respectively, the pore permeability of the F5 fault remains relatively high, allowing some CO₂ to still leak through the fault

Therefore, in the evaluation of appropriate CO_2 injection sites within complex fault-blocks, it is imperative to account for the structure characteristics and the physical properties of the faults on CO_2 transport and storage. This holistic assessment enables the identification of appropriate CO_2 reservoirs and injection sites,

thereby mitigating the potential occurrence of CO_2 leakage (Table 3).

5.2. Control of CO₂ geological storage by different injection sites

The research results of Foroutan and Wang indicate that, The choice of injection site has a very important influence on the effect of CO_2 geological storage (Foroutan et al., 2022; Wang et al., 2023), which is determined by the temperature and pressure of the injection site, the physical characteristics of the reservoir and cap layer, and different geological structure patterns. Although scholars have done a lot of research on the temperature and pressure, physical properties of reservoir and cap layers and geological features. In the actual CO_2 geological storage project, the transportation, dissolution and storage of CO_2 are often determined by these three conditions together. It is of great significance to explore the effect of the coupling of these three conditions on the geological storage of CO_2 .

5.2.1. Temperature and pressure

When the CO₂ injection sites change, temperature and pressure gradients cause the formation temperature and pressure to

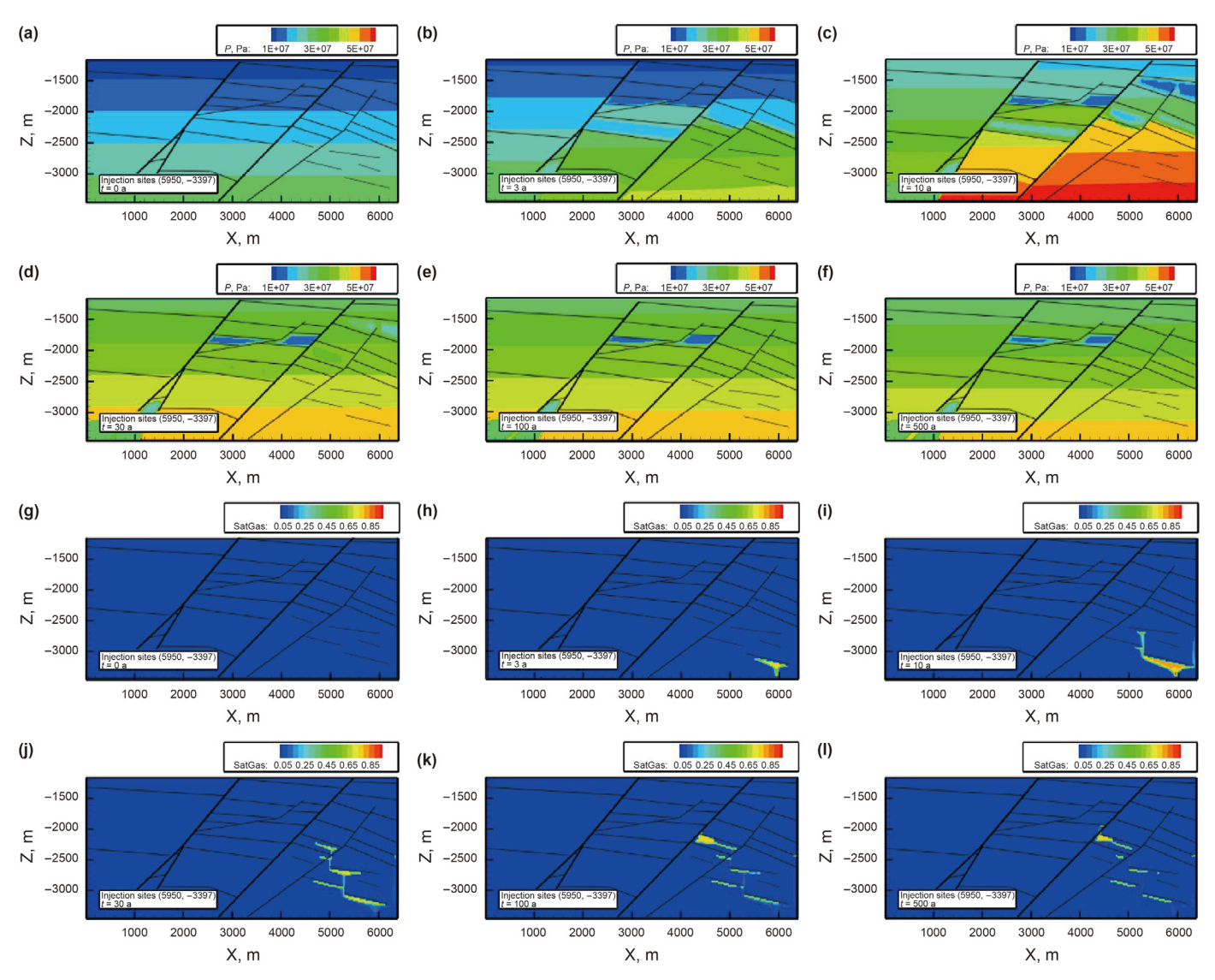


Fig. 9. The formation pressure and CO_2 migration at the injection site (5950, -3397).

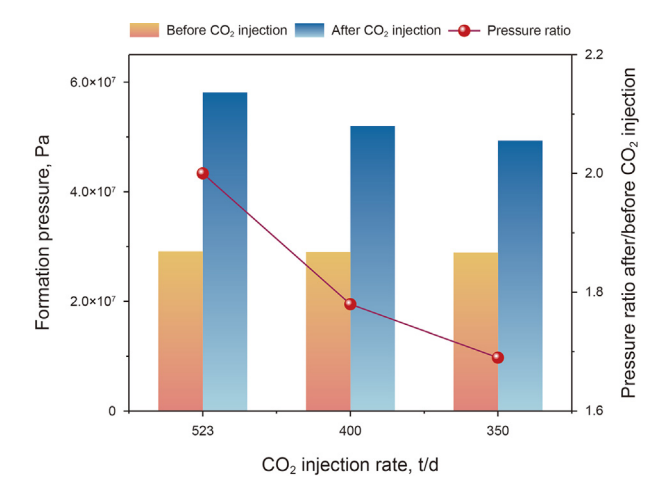


Fig. 10. Formation pressure and pressure ratio before and after ${\rm CO_2}$ injection at different injection rates.

increase as the injection site goes deeper. The study of Han et al. (2023) showed that the increase significantly reduces the storage of CO_2 in the subsurface in the form of adsorption storage. In contrast, Jingjing's study showed that an increase in temperature significantly increases the likelihood of CO_2 leakage along fractures, and the time it takes for CO_2 to break through a fault and leak is greatly reduced (Jing et al., 2019). With the passage of time, CO_2 in the formation gradually changes from the supercritical phase to the dissolved phase, the dissolved phase as a more stable form of storage of CO_2 in the formation, the more it accounts for, indicating that the stronger the security of CO_2 geological storage.

The amount of CO_2 dissolved depends on two aspects: (1) the rate of CO_2 dissolution in formation water; (2) the extent of CO_2 transport. Temperature and pressure have a significant impact on the dissolution rate of CO_2 . In the T-P range covered by our model, the solubility of CO_2 increases with pressure. And for temperature, in a CO_2 saline system at low pressure (<100 bar), the solubility of CO_2 decreases with increasing temperature, while in a high-pressure system (>100 bar), the solubility of CO_2 first decreases with increasing temperature and then increases with increasing

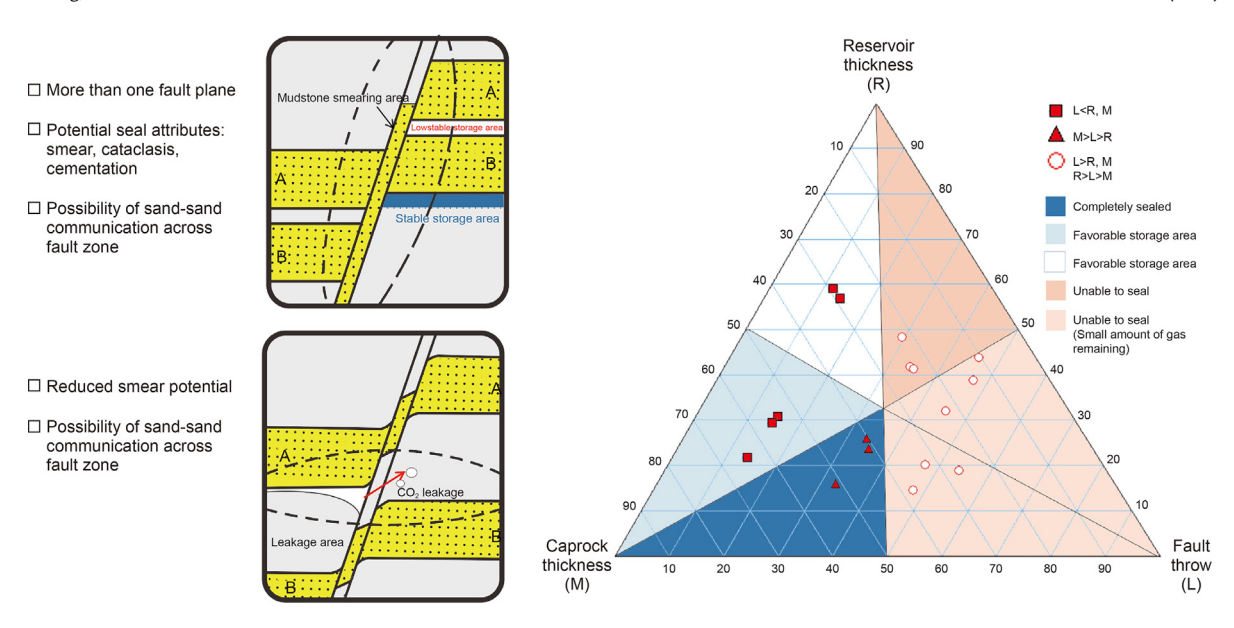


Fig. 11. Block sealing evaluation mode and triangle diagram with different fault throw, reservoir thickness and caprock thicknesses.

Table 3Fault characteristics and CO₂ storage affected by three factors: fault throw (L), reservoir thickness (R), and caprock thickness (M).

Fault properties	L-R-M three-element coupling	Fault characteristic	CO ₂ storage situation
Faults with good physical property	R > L > M	Sandstone-sandstone connection on both sides of the fault	Unable to storage CO ₂
Sealing fault	R, M > L $R > L > M$	Sandstone-mudstone connection on both sides of the fault Sandstone-sandstone connection on both sides of the fault	Partial storage of CO ₂ Partial storage of CO ₂
-	R, M > L	Sandstone-mudstone connection on both sides of the fault	Stabilization of CO ₂ storage

temperature. The isobaric minimum solubility points vary from about 423 K at 100 bar to about 353 K at high pressures (Bando et al., 2003; Bhattacherjee et al., 2023; Duan and Sun, 2003). In this study, the isobaric minimum solubility point is 333.15 K. When the formation temperature is below 333.15 K, the solubility of CO₂ increases with decreasing temperature. Overall, as CO₂ migrates upwards, although the decrease in temperature has a certain promoting effect on the increase of CO₂ solubility, the overall solubility of CO₂ shows a decreasing trend due to the decrease in pressure.

When the extent of CO_2 transport is faster, the higher total volume of CO_2 in which it can be dissolved. There are two main factors that affect CO_2 transport: (1) formation pressure; (2) molecular diffusion. CO_2 transport is described with a multiphase extension of Darcy's law. Therefore, when CO_2 injection leads to formation overpressure, the CO_2 transport rate increases, and the higher the formation pressure, the faster the CO_2 transport rate.

Molecular diffusion has a smaller effect on CO_2 transport compared to pressure and plays a dominant role when the pressure drive is not significant. According to previous research (Cadogan et al., 2014; Omrani et al., 2022), pressure has no significant effect on diffusion coefficient in low-temperature systems. Moultos's (Moultos et al., 2014) research suggests that as temperature increases, the effect of pressure on diffusion coefficient becomes more pronounced. But when the temperature is below 473.15 K, the effect of pressure changes on the diffusion coefficient can be ignored. Therefore, for this study, the supercritical CO_2 diffusion coefficient is more controlled by temperature. The higher the formation temperature, the faster the diffusion rate. In summary, when the depth of the injection site is deeper and the temperature and pressure are higher, it is more favorable for the dissolution and transport of CO_2 .

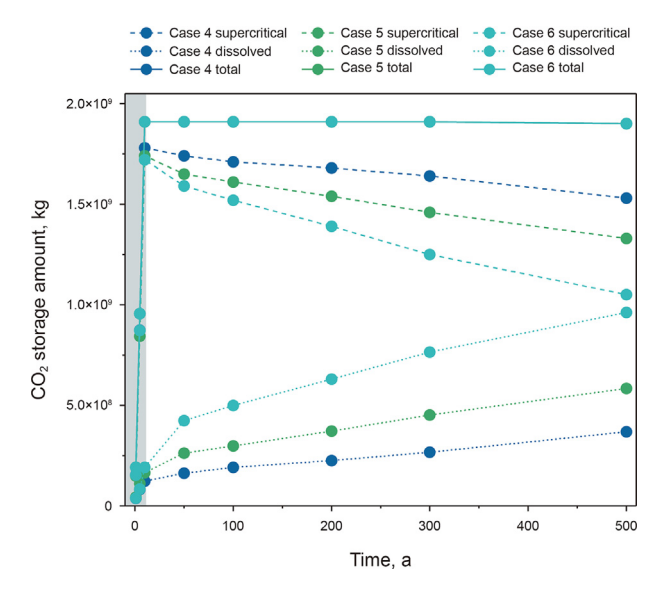
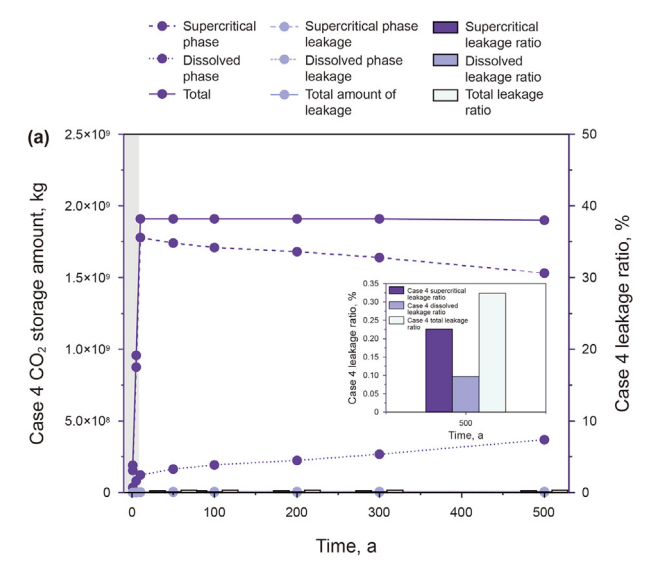
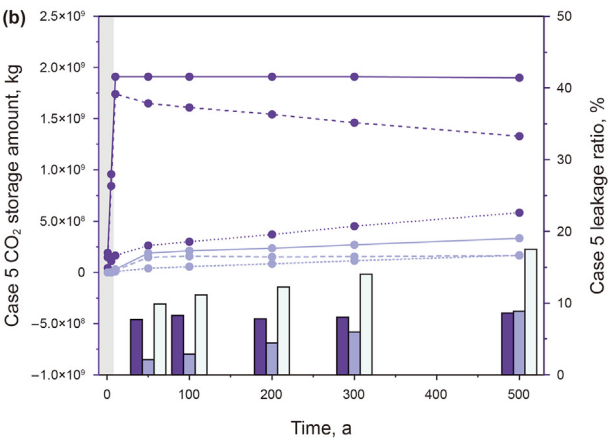


Fig. 12. Variation of the amount and total amount of CO₂ in supercritical and dissolved phase at different injection sites.

The injection sites temperature for Cases 4–6 are 64, 85 and 102 °C, and the pressures are 24, 32 and 38 MPa, respectively. As evidenced in Fig. 12, Case 6 exhibits enhanced dissolution trapping efficiency, achieving 4.23×10^8 kg of dissolved phase CO₂ storage within the initial 50-year period, 61.5% higher than Case 5. Elevated pressure regimes demonstrate a significant positive correlation with CO₂ dissolution kinetics. Notably, temporal analysis reveals distinct dissolution regimes: rapid CO₂ dissolution dominates 0–50





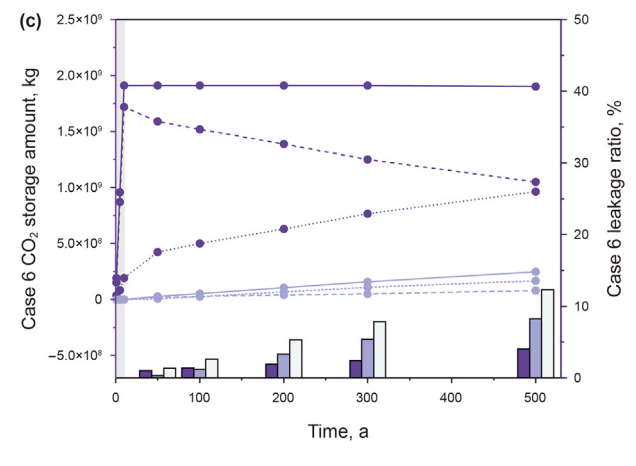


Fig. 13. The amount of CO_2 leakage and storage at different injection sites and the ratio of the amount of leakage to the total amount of CO_2 . (a) injection site (3700, -2166), (b) injection site (6110, -2839), (c) injection site (5950, -3397).

years and followed by asymptotic stabilization during 50–500 years. The cumulative dissolved mass increases merely 18.0% (Case 6: 0.76×10^8 kg) and 12.4% (Case 5: 0.37×10^8 kg) in later stages, indicating near-saturation limits under prolonged geological timescales. These findings underscore the critical trade-off between injection pressure optimization (for short-term dissolution enhancement) and reservoir capacity constraints (governing long-

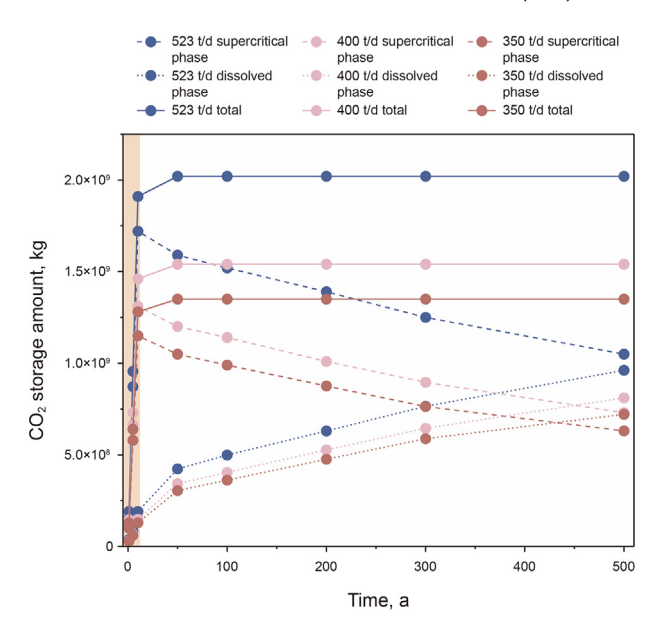


Fig. 14. Changes in the amount and total amount of CO_2 supercritical phase and dissolved phase at different injection rates.

term storage security). At 500 years, the amount of dissolved CO_2 in Case 6 was the highest, reaching 9.62×10^8 kg, while the amount of dissolved CO_2 in Case 5 was 5.83×10^8 kg. In comparison, the injection site in Case 6 was more favorable for CO_2 storage.

5.2.2. CO₂ leakage

 CO_2 leakage is a significant concern in CO_2 geologic storage. Identifying the extent of CO_2 leakage and understanding its pattern are crucial. There are typically two mechanisms through which CO_2 can infiltrate low porosity and low-permeability caprocks and faults (Ali et al., 2023; Hou et al., 2022; Wollenweber et al., 2010). The first mechanism involves the diffusion of dissolved CO_2 into the caprocks and faults via molecular diffusion, driven by concentration gradients. The second mechanism occurs when the capillary resistance of the caprock is overcome, allowing CO_2 and reservoir water to enter the caprock and faults in a two-phase fluid manner. When CO_2 accumulates beneath low porosity and low-permeability faults, its migration is governed by both capillary pressure and molecular diffusion. This leads to the passage of CO_2 through the fault in both supercritical and dissolved phases, ultimately resulting in leakage (Aminu et al., 2017).

Fig. 13(a)–(c) shows the quantities of CO₂ leaked in the supercritical phase, dissolved phase, and the percentage of CO₂ leakage relative to the total amount of CO₂ injected at different injection sites. In Case 4 (Fig. 13), where CO₂ was injected below the F3 sandstone-sandstone connection fault, there was no leakage due to good fault stability. However, in Case 5 and Case 6, CO2 was injected below the F5 sandstone-mudstone connection fault with favorable physical properties and the F4 sandstone-sandstone connection sealing fault, respectively, resulting in some degree of leakage at the fault (Figs. 8(1)-9(1)). The amount of leakage in Case 5 and Case 6 was 3.34×10^8 kg and 2.48×10^8 kg, accounting for 17.5% and 12.3% of the total injection amount, respectively (Fig. 13(b)-(c)). This phenomenon can be attributed to the slower diffusion of CO2 resulting from the F4 fault, characterized by lower porosity and permeability than F5 fault. These findings suggest that the physical property of the fault has a greater impact on the amount of CO₂ leakage compared to the structural form of the fault.

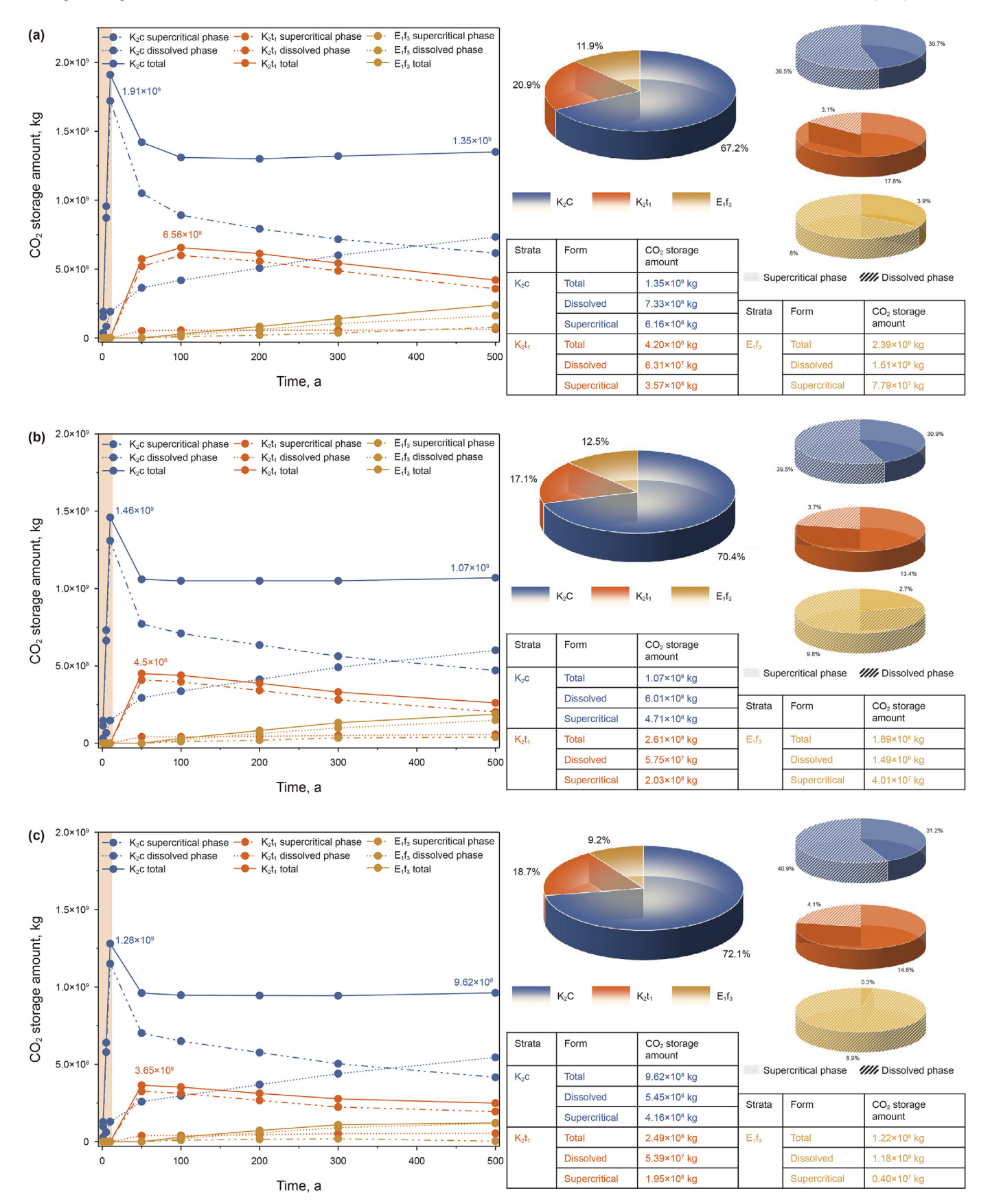


Fig. 15. Enrichment of different strata at 500 years under different CO₂ injection rates, (a) 523 t/d, (b) 400 t/d, (c) 350 t/d.

The CO₂ plume exhibited structural entrapment beneath the F5 fault zone and K_2t_2 caprock, with initial leakage predominantly occurring through supercritical-phase buoyancy-driven migration. CO_2 leakage phase fractions transition revealed a progressive shift from supercritical-phase to dissolved-phase transport: supercritical CO_2 decreased from 8.27% (0–100 a) to 7.83% (100–200 a), while dissolved-phase increased from 2.88% to 4.43%. This suggests the need for early-stage actions to mitigate the harm caused by supercritical CO_2 leakage during CO_2 injection. Finally, after 500 years, the amount of CO_2 in the supercritical phase and dissolved phase was 1.65×10^8 and 1.70×10^8 kg, respectively, accounting for 8.65% and 8.88% of the total CO_2 .

In Case 6 (Fig. 13(c)), distinct migration patterns emerged due to the lower injection sites and the presence of interlayers, delaying CO $_2$ arrival at the F4 fault-K $_2$ t $_2$ caprock interface by 100 years. After 500 years, the amounts of CO $_2$ in supercritical phase leakage were 8.19 \times 10 7 kg (4.06%), while the dissolved phase were 1.66 \times 10 8 kg (8.83%). This indicates that the larger reservoir space and the presence of an interlayer result in a longer range and time for CO $_2$ migration. The resultant prolonged residence time facilitated enhanced CO $_2$ phase transition efficiency, and the proportion of supercritical phase is lower when CO $_2$ reaches and breaks through faults, reducing the risk of CO $_2$ leakage.

5.3. Control of CO₂ capture and leakage by different injection rates

The injection rate is a crucial factor that affects the effectiveness of CO₂ geological storage. The magnitude of the injection rate directly impacts the migration distance of the plume and the capture of CO₂. Research has shown that a higher injection rate results in a greater migration distance for CO₂ and an increased amount of dissolved phase storage (Zhang et al., 2023). However, in the case of complex fault-blocked geologic bodies, the influence of CO₂ transport by the fault structure and the non-homogeneous nature of the geological structure and stratigraphic properties make the impact of different injection rates on CO₂ transport more complex than a simple diffusion problem (Obi and Blunt, 2006; Ehsan et al., 2010; Lengler et al., 2010). Therefore, the discussion on the effect of CO₂ transport and the final capture of CO₂ must be based on the actual geologic conditions.

In this study, we conducted simulations using three different injection rates: 523, 400, and 350 t/d. When CO₂ migrates within the geological body of a fault-block, although the faults act as effective confinement, CO₂ leakage along the faults remains a significant issue in the process (Wang et al., 2023). Therefore, it is crucial to maintain a safe injection rate to prevent CO₂ breakthrough the fault and leakage. As depicted in Fig. 9(1) and Fig. S2(1), as the injection rate decreases, the likelihood of CO₂ breakthrough and upward transport diminishes. Ultimately, when the injection rate reaches 350 t/d, the CO₂ accumulates and seals near the fault.

As shown in Fig. 14, When the injection rate decreases, the total amount of dissolved phase CO₂ decreases, but the percentage of dissolved phase CO₂ in the total CO₂ gradually increases. At 500 years, when the injection rate was 523 t/d, the content of the dissolved phase of CO₂ was 9.62×10^8 kg, which was close to the content of the supercritical phase of 1.05×10^9 kg, but when the injection rate decreased to 400 t/d and 350 t/d, the content of the dissolved phase exceeded the supercritical phase, reaching 8.11×10^8 and 7.21×10^8 kg, respectively. Therefore, a higher injection rate does increase a higher amount of dissolved CO₂ storage, but reducing the injection rate can enhance the conversion of supercritical CO₂ into dissolved CO₂, improving storage efficiency.

The migration path following CO_2 injection proceeds initially in the K_2c reservoir, then transitions to the K_2t_1 reservoir, and

ultimately traverses the F4 fault to reach the E₁f₃ reservoir. After the CO₂ breaks through the F4 fault and enters the E₁f₃ reservoir, this study examines the storage of CO2 and the proportion of supercritical-dissolved two-phase in each formation along the migration path. The monitoring results of the supercritical phase and dissolved phase of E₁f₃, at different injection rates, demonstrate that the amount of CO2 in the supercritical phase that penetrates the F4 fault and enters E₁f₃ decreases as the injection rate decreases. Specifically, the proportion of supercritical phase are 3.9%, 2.7%, and 0.3% respectively. In contrast, the dissolved phase remains relatively stable, with the proportion of 8.0%, 9.8%, and 8.9% respectively (Fig. 15(a)-(c)). By reducing the leakage of supercritical CO₂, the risks and hazards associated with CO₂ leakage along faults are significantly mitigated (Wang et al., 2023). When the injection rate is reduced to 350 t/d, the amount of supercritical CO₂ leakage becomes negligible, making it a safe injection rate.

6. Conclusion

- (1) Fault structure plays a decisive role in the storage of CO₂ in complex fault-block geological bodies, which depends on the coupling relationship of the three factors of 'fault throw-reservoir thickness-caprock thickness'. In the synthetic faults, when the fault throw is less than the thickness of the reservoir and the thickness of the caprocks, the two sides of the fault are sandstone and mudstone respectively, and the CO₂ storage effect is good. On the contrary, when the fault throw is greater than the thickness of the caprock but less than the reservoir thickness, the fault's two sides are connected by sandstone formations, and the CO₂ storage effect is poor. Sealing faults caused by mudstone smearing have a certain enhancement effect on CO₂ storage.
- (2) The position at which CO₂ is injected directly impacts the CO₂ storage, leakage, and distribution of formation pressure. As the injection site gets deeper, the formation temperature and pressure increase, resulting in a faster dissolution and diffusion rate of CO₂. When the injection of CO₂ is located below the F4 or F5 fault, after 500 years, approximately 17.5% and 12.3% of the total injected amount respectively leak. The larger reservoir space and the presence of an interlayer extends CO₂ migration timescales to faults by 120–150 years, facilitating phase transition from supercritical to dissolved phase.
- (3) The injection rate is a crucial factor in controlling the migration and storage of CO₂. In fault-block geological bodies, a lower injection rate leads to a higher proportion of dissolved CO₂ and smaller CO₂ leakage, making the storage of CO₂ safer. When the CO₂ injection rate is 523, 400, and 350 t/d, the proportion of dissolved phase CO₂ is 36.5%, 39.5%, and 40.9%. The proportion of CO₂ supercritical phase leakage is 3.9%, 2.7%, and 0.3%, respectively. The risk of leakage decreases as the injection rate decreases.

CRediT authorship contribution statement

Zi-Yang Song: Writing — original draft, Software, Methodology, Formal analysis, Data curation, Conceptualization. **Lei-Lei Yang:** Writing — review & editing, Validation, Supervision, Resources, Conceptualization. **Yi Liu:** Methodology. **Fu-Jie Jiang:** Supervision, Investigation. **Xiao-Feng Li:** Supervision. **Zhen-Guo Qi:** Resources, Investigation. **Zhen-Yuan Yin:** Methodology.

Declaration of interests

The authors declare that they have no known competing financial interests or personal relationships that could have appeared to influence the work reported in this paper.

Acknowledgments

This work is granted by the Beijing Natural Science Foundation (No. 8232044), and the Science Foundation of China University of Petroleum, Beijing (No.2462023BJRC030).

Appendix A. Supplementary data

Supplementary data to this article can be found online at https://doi.org/10.1016/j.petsci.2025.03.018.

References

- Ali, F., Negash, B.M., Ridha, S., Abdulelah, H., 2023. A review on the interfacial properties of caprock/CO₂/brine system-implications for structural integrity of deep saline aquifers during geological carbon storage. Earth Sci. Rev. 247, 104600. https://doi.org/10.1016/j.earscirev.2023.104600.
- Aminu, M.D., Nabavi, S.A., Rochelle, C.A., Manovic, V., 2017. A review of developments in carbon dioxide storage. Appl. Energy 208, 1389–1419. https://doi.org/10.1016/j.apenergy.2017.09.015.
- Bando, S., Takemura, F., Nishio, M., Hihara, E., Akai, M., 2003. Solubility of CO₂ in aqueous solutions of NaCl at (30 to 60) °C and (10 to 20) MPa. J. Chem. Eng. Data 48, 576–579. https://doi.org/10.1021/je0255832.
- Bhattacherjee, R., Botchway, K., Pashin, J.C., Chakraborty, G., Bikkina, P., 2023. Machine learning-based prediction of CO₂ fugacity coefficients: application to estimation of CO₂ solubility in aqueous brines as a function of pressure, temperature, and salinity. Int. J. Greenh. Gas Control 128, 103971. https://doi.org/10.1016/j.ijggc.2023.103971.
- Bu, F., Xu, T., Wang, F., Yang, Z., Tian, H., 2016. Influence of highly permeable faults within a low-porosity and low-permeability reservoir on migration and storage of injected CO₂. Geofluids 16 (4), 653–798. https://doi.org/10.1111/gfl.12185.
- Cadogan, S.P., Maitland, G.C., Trusler, J.P.M., 2014. Diffusion coefficients of CO₂ and N₂ in water at temperatures between 298.15 K and 423.15 K at pressures up to 45 MPa. J. Chem. Eng. Data 59, 519–525. https://doi.org/10.1021/je401008s.
- Chen, X.S., Li, Y.P., Jiang, Y.L., Liu, Y.X., Zhang, T., 2022. Theoretical research on gas seepage in the formations surrounding bedded gas storage salt cavern. Pet. Sci. 19, 1766–1778. https://doi.org/10.1016/j.petsci.2022.01.021.
- Chen, F.X., Wang, Y.W., Bi, R., Pan, Y.W., Wang, M., 2024. Molecular insights into CO₂ enhanced hydrocarbon recovery and its sequestration in multiscale shale reservoirs. Chem. Eng. J. 498. https://doi.org/10.1016/j.cej.2024.155913.
- Ciftci, N.B., Giger, S.B., Clennell, M.B., 2013. Three-dimensional structure of experimentally produced clay smears: implications for fault seal analysis. Am. Assoc. Petrol. Geol. Bull. 97, 733–757. https://doi.org/10.1306/10161211192.
- Duan, Z.H., Sun, R., 2003. An improved model calculating CO₂ solubility in pure water and aqueous NaCl solutions from 273 to 533 K and from 0 to 2000 bar. Chem. Geol. 193, 257–271. https://doi.org/10.1016/S0009-2541(02)00263-2.
- Ehsan, S., Steven, L.B., Kamy, S., 2010. New Trapping Mechanism in Carbon Sequestration, vol. 82. Transp Porous Media. https://doi.org/10.1007/s11242-
- Emad, A.A.K., Stephanie, V., Ahmed, B., Mohammad, S., Stefan, I., 2018a. Effect of wettability heterogeneity and reservoir temperature on CO₂ storage efficiency in deep saline aquifers. Int. J. Greenh. Gas Control 68. https://doi.org/10.1016/ j.ijggc.2017.11.016.
- Emad, A.A.K., Stephanie, V., Ahmed, B., Mohammad, S., Yihuai, Z., Stefan, I., 2018b. Impact of salinity on CO₂ containment security in highly heterogeneous reservoirs. Greenhouse Gases: Sci. Technol. 8. https://doi.org/10.1002/ghg.1723.
- Erlend, H., Sarah, G., Roland, K., Tor, C.B., Christian, H., Kirsti, M., 2019. Effect of temperature and concentration of impurities in the fluid stream on CO₂ migration in the Utsira formation. Int. J. Greenh. Gas Control 83. https://doi.org/ 10.1016/j.ijggc.2019.01.020.
- Foroutan, M., Ghazanfari, E., Amirlatifi, A., Moradian, O., 2022. Evolution of fracture permeability and aperture during CO₂ storage in varyingly cemented sedimentary rocks. Geomech. Energy Environ. 32, 100289. https://doi.org/10.1016/i.gete.2021.100289.
- Gao, G., Yang, S.R., Zhang, W.W., Wang, Y., Gang, W.Z., Lou, G.Q., 2018. Organic geochemistry of the lacustrine shales from the cretaceous Taizhou Formation in the Gaoyou sag, northern Jiangsu Basin. Mar. Petrol. Geol. 89. https://doi.org/10.1016/j.marpetgeo.2017.10.023.
- Gershenzon Jr., N.I., Ritzi, R.W., Dominic, D.F., Soltanian, M., Mehnert, E., Okwen, R.T., 2015. Influence of small-scale fluvial architecture on CO₂ trapping processes in deep brine reservoirs. Water Resour. Res. 51, 8240–8256. https://doi.org/10.1002/2015WR017638.

- Gherardi, F., Xu, T., Pruess, K., 2007. Numerical modeling of self-limiting and self-enhancing caprock alteration induced by CO2 storage in a depleted gas reservoir. Chem. Geol. 244 (1–2), 103–129. https://doi.org/10.1016/j.chemgeo.2007.06.009.
- Han, S.J., Sang, S.X., Duan, P.P., Zhang, J.C., Xiang, W.X., Xu, A., 2022. The effect of the density difference between supercritical CO₂ and supercritical CH₄ on their adsorption capacities: an experimental study on anthracite in the Qinshui Basin. Pet. Sci. 19, 1516–1526. https://doi.org/10.1016/j.petsci.2022.03.003.
- Han, S.J., Sang, S.X., Zhang, J., Xiang, W., Xu, A., 2023. Assessment of CO₂ geological storage capacity based on adsorption isothermal experiments at various temperatures: a case study of No. 3 coal in the Qinshui Basin. Petroleum 9, 274–284. https://doi.org/10.1016/j.petlm.2022.04.001.
- Haszeldine, R.S., 2006. Deep geological CO₂ storage: principles reviewed, and prospecting for bio-energy disposal sites. Mitig. Adapt. Strategies Glob. Change 11 (2), 369–393. https://doi.org/10.1007/s11027-005-9005-6.
- Hou, L., Yu, Z., Luo, X., Wu, S., 2022. Self-sealing of caprocks during CO₂ geological sequestration. Energy 252, 124064. https://doi.org/10.1016/ j.energy.2022.124064.
- Jing, J., Yang, Y.L., Tang, Z.H., 2019. Effects of formation dip angle and salinity on the safety of CO₂ geological storage - a case study of Shiqianfeng strata with low porosity and low permeability in the Ordos Basin, China. J. Clean. Prod. 226. https://doi.org/10.1016/j.jclepro.2019.04.038.
- Jing, J., Yang, Y., Cheng, J., Ding, Z., Wang, D., Jing, X., 2023. Analysis of the effect of formation dip angle and injection pressure on the injectivity and migration of CO₂ during storage. Energy 280. https://doi.org/10.1016/j.energy.2023.128021.
- CO₂ during storage. Energy 280. https://doi.org/10.1016/j.energy.2023.128021.

 Johannes, M.M., Stuart, M.V.G., Norbert, F., Andrea, S., Neil, M.B.R.S.H., 2019. 420000 year assessment of fault leakage rates shows geological carbon storage is secure. Sci. Rep. 9, 769. https://doi.org/10.1038/s41598-018-36974-0.
- Lengler, U., Lucia, M.D., 2010. The impact of heterogeneity on the distribution of CO₂: Numerical simulation of CO₂ storage at Ketzin. Int. J. Greenh. Gas Control. 4 (6), 1016–1025. https://doi.org/10.1016/j.ijggc.2010.07.004.
- Li, Y., Xu, C.L., Zhu, J.X., Lu, H.F., Liu, Y.T., Gu, Y.H., Pan, Z.J., Linga, P., Yin, Z.Y., 2024a. Comprehensive characterizations of core sediments recovered from Shenhu W17 well in South China sea and its impact on methane hydrate kinetics. Gas Sci. Eng. 131. https://doi.org/10.1016/j.igsce.2024.205482.
- Sci. Eng. 131. https://doi.org/10.1016/j.jgsce.2024.205482.
 Li, Y., Yin, Z.Y., Rao, Y.Z., Lu, H.F., Xu, C.L., Liu, X.J., Li, Y., Zhao, J.Z., Linga, P., 2024b.
 Ultrarapid CO₂ hydrate nucleation and growth enabled by magnesium coupled with amino acids as a promoter. Energy Fuels 38 (17), 16543—16554. https://doi.org/10.1021/acs.energyfuels.4c01776.
- Liu, C., Xie, Q.B., Wang, G.W., Zhang, C.J., Wang, L.L., Qi, K.N., 2016. Reservoir properties and controlling factors of contact metamorphic zones of the diabase in the northern slope of the Gaoyou Sag, Subei Basin, eastern China. J. Nat. Gas Sci. Eng. 35, 392–411. https://doi.org/10.1016/j.jngse.2016.08.070.
- Liu, S.Y., R, B., Li, H.Y., Yang, Y.Z., Wang, Z.Q., Wang, B., Xu, J.C., Agarwal, R., 2021. CO₂ storage with enhanced gas recovery(CSEGR): a review of experimental and numerical studies. Pet. Sci. 19, 594–607. https://doi.org/10.1016/j.petsci.2021.12.009.
- Liu, Y., Rui, Z., Yang, T., Dindoruk, B., 2022. Using propanol as an additive to CO₂ for improving CO₂ utilization and storage in oil reservoirs. Appl. Energy 311. https://doi.org/10.1016/j.apenergy.2022.118640.
- Moultos, O.A., Tsimpanogiannis, I.N., Panagiotopoulos, A.Z., Economou, I.G., 2014. Atomistic molecular dynamics simulations of CO₂ diffusivity in H₂O for a wide range of temperatures and pressures. J. Phys. Chem. B 118, 5532–5541. https://doi.org/10.1021/jp502380r.
- Noorsalehi-Garakani, S., Kleine Vennekate, G.J., Vrolijk, P., Urai, J.L., 2013. Claysmear continuity and normal fault zone geometry first results from excavated sandbox models. J. Struct. Geol. 57, 58–80. https://doi.org/10.1016/j.jsg.2013.09.008.
- Obi, E.O.I., Blunt, M.J., 2006. Streamline-based simulation of carbon dioxide storage in a North Sea aquifer. Water Resour. Res. 42, 3411–3414. https://doi.org/ 10.1029/2004WR003347.
- Omrani, S., Ghasemi, M., Mahmoodpour, S., Shafiei, A., Rostami, B., 2022. Insights from molecular dynamics on CO₂ diffusion coefficient in saline water over a wide range of temperatures, pressures, and salinity: CO₂ geological storage implications. J. Mol. Liq. 345, 117868. https://doi.org/10.1016/j.molliq.2021.117868.
- Pacala, S., Socolow, R., 2004. Stabilization wedges: solving the climate problem for the next 50 Years with current technologies. Science 305 (5686), 968–972. https://doi.org/10.1126/science.1100103.
- Pruess, K., Spycher, N., 2007. ECO2N a fluid property module for the TOUGH2 code for studies of CO₂ storage in saline aquifers. Energy Convers. Manag. 48, 1761–1767. https://doi.org/10.1016/j.enconman.2007.01.016.
- Punnam, P.R., Krishnamurthy, B., Surasani, V.K., 2022. Investigation of solubility trapping mechanism during geologic CO₂ sequestration in Deccan Volcanic Provinces, Saurashtra, Gujarat, India. Int. J. Greenh. Gas Control 120, 103769. https://doi.org/10.1016/j.ijggc.2022.103769.
- Qiao, X., Li, G.M., Li, M., Wang, Z.M., 2012. CO₂ storage capacity assessment of deep saline aquifers in the Subei Basin, East China. Int. J. Greenh. Gas Control 11, 52–63. https://doi.org/10.1016/j.ijggc.2012.07.020.
- Qin, J., Zhong, Q., Tang, Y., Rui, Z., Qiu, S., Chen, H., 2023. CO₂ storage potential assessment of offshore saline aquifers in China. Fuel 341, 127681. https://doi.org/10.1016/j.fuel.2023.127681.
- Rae, J.W.B., Burke, A., Robinson, L.F., Adkins, J.F., Chen, T., Cole, C., Greenop, R., Li, T., Littley, E.F.M., Nita, D.C., Stewart, J.A., Taylor, B.J., 2018. CO₂ storage and release

- in the deep Southern Ocean on millennial to centennial timescales. Nature 562, 569–573, https://doi.org/10.1038/s41586-018-0614-0.
- Shabani, B., Vilcáez, J., 2018. A fast and robust TOUGH2 module to simulate geological CO₂ storage in saline aquifers. Comput. Geosci. 111, 58–66. https:// doi.org/10.1016/j.cageo.2017.10.012.
- Song, Z.Y., Yang, L.L., Jiang, F.J., Zhu, W.C., Li, X.F., Qi, Z.G., Yin, Z.Y., 2024. The mechanism of clay mineral transformation in CO₂ geological storage and its impact on long-term storage potential. Geoenergy Sci. Eng. 242, 213192. https:// doi.org/10.1016/j.geoen.2024.213192.
- Spycher, N., Pruess, K., 2005. CO₂-H₂O mixtures in the geological sequestration of CO₂. II. Partitioning in chloride brines at 12–100 °C and up to 600 bar. Geochem. Cosmochim. Acta. 69, 3309–3320. https://doi.org/10.1016/j.gca.2005.01.015.
- Tang, Y., Hou, C., He, Y., Wang, Y., Chen, Y., Rui, Z., 2020. Review on pore structure characterization and microscopic flow mechanism of CO₂ flooding in porous media. Energy Technol. 9 (1), 2000787. https://doi.org/10.1002/ente.202000787.
- Wang, C., Wang, W., Su, Y., Zhao, Y., Wen, J., Li, L., Hao, Y., 2023. Assessment of CO₂ storage potential in high water-cut fractured volcanic gas reservoirs—case study of China's SN gas field. Fuel 335, 126999. https://doi.org/10.1016/j.fuel.2022.126999.
- Wang, H., Kou, Z., Ji, Z., Wang, S., Li, Y., Jiao, Z., Johnson, M., McLaughlin, J.F., 2023. Investigation of enhanced CO₂ storage in deep saline aquifers by WAG and brine extraction in the Minnelusa sandstone, Wyoming. Energy 265 (15), 126379. https://doi.org/10.1016/j.energy.2022.126379.
- Wang, Z., Li, H., Liu, S., Xu, J., Liu, J., Wang, X., 2023a. Risk evaluation of CO₂ leakage through fracture zone in geological storage reservoir. Fuel 342, 127896. https:// doi.org/10.1016/j.fuel.2023.127896.
- Wang, Y.W., Chu, H., Lyu, X., 2024a. Deep learning in CO₂ geological utilization and storage: recent advances and perspectives. Adv. Geo-Energy Res. 13 (3), 161–165. https://doi.org/10.46690/ager.2024.09.01.
- Wang, Y.W., Dai, Z.X., Wang, G.S., Chen, L., Xia, Y.Z., Zhou, Y.H., 2024b. A hybrid physics-informed data-driven neural network for CO₂ storage in depleted shale reservoirs. Pet. Sci. 21 (1), 286–301. https://doi.org/10.1016/j.petsci.2023.08.032.
- Wen, G., Tang, M., Benson, S.M., 2021. Towards a predictor for CO₂ plume migration using deep neural networks. Int. J. Greenh. Gas Control 105, 103223. https://doi.org/10.1016/j.ijggc.2020.

- Wollenweber, J., Alles, S., Busch, A., Krooss, B.M., Stanjek, H., Littke, R., 2010. Experimental investigation of the CO₂ sealing efficiency of caprocks. Int. J. Greenh. Gas Control 4, 231–241. https://doi.org/10.1016/j.ijggc.2010.01.003.
- Xu, T.F., Sonnenthal, E., Spycher, N., Pruess, K., 2006. Toughreact a simulation program for non-isothermal multiphase reactive geochemical transport in variably saturated geologic media: applications to geothermal injectivity and CO₂ geological sequestration. Comput. Geosci. 32 (2), 145–165. https://doi.org/10.1016/j.cageo.2005.06.014.
- Yang, F., Bai, B., Tang, D., Shari, D.N., David, W., 2010. Characteristics of CO₂ sequestration in saline aquifers. Pet. Sci. 7, 83–92. https://doi.org/10.1007/s12182-010-0010-3.
- Yang, Y.L., Xu, T.F., Bu, F.T., Lei, H.W., Shi, Y., Jin, G.R., Wang, F.G., 2013. TOUGHVISUAL A friendly graphical user interface for building TOUGHREACT models under complex 3D geological environments. In: Proceedings of the 2013 International Conference on Software Engineering and Computer Science. https://doi.org/ 10.2991/ICSECS-13.2013.20.
- Yang, Z.J., Xu, T.F., Wang, F.G., Yang, Y.L., Li, X.F., Zhao, N.N., 2018. Impact of inner reservoir faults on migration and storage of injected CO₂. Int. J. Greenh. Gas Control 72, 14–25. https://doi.org/10.1016/j.ijggc.2018.03.006.
 Yang, L.L., Song, Z.Y., Liu, Y., Wei, G., Zhang, X., Mo, C.C., Feng, B., Li, Y.H., 2023.
- Yang, L.L., Song, Z.Y., Liu, Y., Wei, G., Zhang, X., Mo, C.C., Feng, B., Li, Y.H., 2023. Differences in CO₂-water-rock chemical reactions among 'sweet spot' reservoirs: implications for carbon sequestration. Acta Geol. Sinica-English Edition 97 (3), 972–985. https://doi.org/10.1111/1755-6724.15076.
- Zhang, D.X., Song, J., 2014. Mechanisms for geological carbon sequestration. Procedia IUTAM 10, 319–327.. https://doi.org/10.1016/j.piutam.2014.01.027.
- Zhang, H., Kobaisi, M.A., Arif, M., 2023. Impact of wettability and injection rate on CO₂ plume migration and trapping capacity: a numerical investigation. Fuel 331 (1), 125721. https://doi.org/10.1016/j.fuel.2022.125721.
- Zhao, J., Li, W., Xiao, H.W., Qi, X.Z., Yuan, S.S., 2018. Numerical simulation and correction of electrical resistivity logging for different formation dip angles. J. Petrol. Sci. Eng. 164, 344–350. https://doi.org/10.1016/j.petrol.2018.01.067.
- Zheng, X., Espinoza, D.N., 2022. Stochastic quantification of CO₂ fault sealing capacity in sand-shale sequences. Mar. Petrol. Geol. 146, 105961. https://doi.org/10.1016/j.marpetgeo.2022.105961.
- Zhou, X.W., Jiang, Z.X., Jonathan, A.Q., Duan, Y., Hu, C.L., Liu, C., Han, C., 2019. Ichnology and sedimentology of the trace fossil-bearing fluvial red beds from the lowermost member of the paleocene Funing Formation in the jinhu depression, Subei Basin, east China. Mar. Petrol. Geol. 99, 393–415. https://doi.org/10.1016/j.marpetgeo.2018.10.032.